China Geology 6 (2023) 303−321

China Geology

Journal homepage: http://chinageology.cgs.cn
https://www.sciencedirect.com/journal/china-geology

The long-lived partial melting of the Greater Himalayas in southern Tibet, constraints from the Miocene Gyirong anatectic pegmatite and its prospecting potential for rare element minerals

Hua-wen Cao[a, b], Qiu-ming Pei[c,*], Xiao Yu[d, e], Ai-bin Cao[d, e], Yong Chen[d], Hang Liu[a, b], Kai Zhang[a, e], Xin Liu[a, e], Xiang-fei Zhang[a, b]

[a] *Chengdu Center, China Geological Survey (Geosciences Innovation Center of Southwest China), Ministry of Natural Resources, Chengdu* 610218, *China*
[b] *College of Earth Sciences, Chengdu University of Technology, Chengdu* 610059, *China*
[c] *Faculty of Geosciences and Environmental Engineering, Southwest Jiaotong University, Chengdu* 611756, *China*
[d] *Research Center of Applied Geology, China Geological Survey, Ministry of Natural Resources, Chengdu* 610036, *China*
[e] *School of Earth Resources, China University of Geosciences, Wuhan* 430074, *China*

ARTICLE INFO

Article history:
Received 25 August 2022
Received in revised form 7 November 2022
Accepted 5 December 2022
Available online 29 March 2023

Keywords:
Partial melting of magma
Anatectic pegmatite
Zircon-monazite-xenotime U–Pb dating
Sr-Nd-Pb isotopes
Greater Himalayan crystalline complex
Mineral exploration engineering
Gyirong
Tibet

ABSTRACT

The Cenozoic Himalayan leucogranite-pegmatite belt has been a hotspot for rare metal exploration in recent years. To determine the genesis of the pegmatite in the Himalayan region and its relationship with the Greater Himalayan Crystalline Complex (GHC), the Gyirong pegmatite in southern Tibet was chosen for geochronological and geochemical studies. The dating analyses indicate that the U-Th-Pb ages of zircon, monazite, and xenotime exhibit large variations (38.6–16.1 Ma), with the weighted average value of the four youngest points is 16.5 ± 0.3 Ma, which indicates that the final stage of crystallization of the melt occurred in the Miocene. The age of the muscovite Ar-Ar inverse isochron is 15.2 ± 0.4 Ma, which is slightly later than the intrusion age, showing that a cooling process associated with rapid denudation occurred at 16–15 Ma. The $\varepsilon_{Hf}(t)$ values of the Cenozoic anatectic zircons cluster between −12 and −9 with an average of −11.4. The Gyirong pegmatite shows high contents of Si, Al, and K, a high Al saturation index, and low contents of Na, Ca, Fe, Mn, P, Mg, and Ti. Overall, the Gyirong pegmatite is enriched in Rb, Cs, U, K, Th and Pb and depleted in Nb, Ta, Zr, Ti, Eu, Sr, and Ba. The samples show a high $^{87}Sr/^{86}Sr_{(16\ Ma)}$ ratio of ca. 0.762 and a low $\varepsilon_{Nd(16\ Ma)}$ value of −16.0. The calculated average initial values of $^{208}Pb/^{204}Pb_{(16\ Ma)}$, $^{207}Pb/^{204}Pb_{(16\ Ma)}$ and $^{206}Pb/^{204}Pb_{(16\ Ma)}$ of the whole rock are 39.72, 15.79 and 19.56, respectively. The Sr-Nd-Pb-Hf isotopic characteristics of the Gyirong pegmatite are consistent with those of the GHC. This study concludes that the Gyirong pegmatite represents a typical crustal–derived anatectic pegmatite with low metallogenic potential for rare metals. The Gyirong pegmatite records the long–term metamorphism and partial melting process of the GHC, and reflects the crustal thickening caused by thrust compression at 39–29 Ma and the crustal thinning induced by extensional decompression during 28–15 Ma.

1. Introduction

Pegmatite is an important source of rare elements, such as Li, Be, Nb, Ta, and rare earth elements (REEs) (Černý R and Ercit TS, 2005; London D, 2018; Li X et al., 2022a). The study of the genesis of pegmatites has important exploration significance and economic value (Zhou W et al., 2022). However, the genetic classification and genesis of pegmatites has long been a controversial aspect of geological research (London D and Kontak DJ, 2012; Dill HG, 2015, 2018). They can be simply divided into anatectic pegmatites related to metamorphic melts and magmatic pegmatites related to magmatic highly differentiated residual melts (Müller A et al., 2022; Wise MA et al., 2022). High-degree partial melting (20%–40%) of crust-derived sedimentary rocks can form the parent magma of a magmatic pegmatite, while low-degree

First author: *E-mail address*: caohuawen1988@126.com (Hua-Wen Cao).
* Corresponding author: *E-mail address*: pqm@swjtu.edu.cn (Qiu-Ming Pei).

Literary editor: Xi-jie Chen
doi:10.31035/cg2022061
2096-5192/© 2023 China Geology Editorial Office.

partial melting (ca. 10%) can form the parent melts of an anatectic pegmatite (Linnen RL et al., 2012; Zhao ZH et al., 2022). Although the metallogenic potential and tectonic significance of these two types of pegmatites are quite different, their differences and similarities are poorly constrained (Müller A et al., 2017).

A large number of Cenozoic leucogranites and pegmatites have developed in the Himalayas (Cao HW et al., 2022a). The origin of the leucogranites has been well documented, and there are two main viewpoints regarding their origin (Cao HW et al., 2022a, 2022b). In one model, the leucogranites are derived from the low-degree partial melting of the middle and lower crust of India, namely the Greater Himalayan Crystalline Complex (GHC) (Le Fort P et al., 1987). In the other model, they are derived from the high differentiation of magmatic melt with small amounts of mantle materials (Wu FY et al., 2020). In addition, the partial melting process can be divided into fluid-present melting and fluid-absent dehydration melting (Gao LE et al., 2017, 2021). It's worth noting that less attention has been given to the pegmatites in the Himalayas (Liu C et al., 2020). The study of the Himalayan pegmatite can provide new evidence for its origin. In addition, there are disputes about the origin of these pegmatites, with proposed hypotheses including the high differentiation of magma or metamorphic remelting (Searle MP et al., 1992; Searle MP, 2019; Bhandari S et al., 2022). During the Miocene, rapid uplift occurred in the Himalayan region (Ding L et al., 2022), and the GHC was exhumed to the upper crust (Kohn MJ, 2014) via denudation and exhumation, which resulted in the large-scale intrusion of leucogranite (Goscombe B et al., 2018) and extensive mineralization of ore deposits rich in Li, Be, W, Sn, Pb, Zn, Ag, Sb and Au (Cao HW et al., 2021). The metamorphism, tectonics, and magmatism during the Cenozoic in the Himalayan have close internal connections (Weinberg RF, 2016). Therefore, the in-depth study of the genesis of Himalayan pegmatites can provide unparalleled insights for the study of the abovementioned Miocene tectonic evolution process and ore-forming process in southern Tibet.

To study the origin of the pegmatites in the Himalayan region and their relationship with the partial melting of the GHC (Zeng LS and Gao LE, 2017; Zhang ZM et al., 2018), a pegmatite sample was collected from the GHC in the Gyirong town for the U-Th-Pb dating of zircon, monazite, and xenotime, the Ar-Ar dating of muscovite, and the Lu-Hf isotope analysis of zircon. Furthermore, six fresh rock samples were collected for the analysis of major and trace elements and Sr-Nd-Pb isotopes in the whole rock. This study aims to document the genesis and tectonic setting of the Miocene anatectic pegmatites in the Himalayas. This contribution indicates that the pegmatites record long-term Eocene-Oligocene prograde metamorphism and Miocene retrograde metamorphism and melt crystallization processes in the GHC, which correspond tectonically to crustal thickening and thinning in the Himalayan region, respectively.

2. Geological setting

From north to south, the Qinghai-Tibet Plateau is composed of the Songpan-Ganze, North Qiangtang, South Qiangtang, Lhasa, and Himalayan (Indian plate) regions (Pan GT et al., 2012, 2022; Yu SM et al., 2022). These blocks are divided by the Jinsha River, Longmu Co-Shuanghu, Bangong Lake-Nujiang and Indus-Yarlung Zangbo suture zones (Yin A, 2006; Xu B et al., 2021a, 2021b; Zhao ZB et al., 2021). The Indus-Yarlung Zangbo suture zone represents the Mesozoic Neo-Tethys Ocean relic between the Indian and Lhasa plates (Metcalfe I, 2021; Xu B et al., 2022). The division between the northern side of the Himalayan orogenic belt and the Lhasa plate is defined by the Indus-Yarlung Zangbo suture zone, and the division between the southern side and the Indian plate (craton) is defined by the Main Frontal Thrust (MFT; Fig. 1). From north to south, the Himalayan terrane is divided into four main tectonic units: the Tethyan Himalayan Sequence (THS), the GHC, the Lesser Himalayan Sequence (LHS) and the sub-Himalayan Sequence (SHS), which are separated by the South Tibet Detachment System (STDS), the Main Central Thrust (MCT) and the Main Boundary Thrust (MBT), respectively (Goscombe B et al., 2018; Wang JM et al., 2022).

The THS comprises the sediments deposited in the passive continental margin sedimentary environment of the Indian plate during the Paleozoic-Mesozoic and contains a set of low-grade metamorphic (low amphibolite-facies) clastic rocks and carbonate rocks (Cao HW et al., 2018). The GHC represents the core of the Himalayan orogenic belt (material from the middle and lower crust) and is composed of Proterozoic–lower Paleozoic sedimentary rock series and magmatic rocks that have generally undergone granulite- to eclogite- facies metamorphism. A set of crystalline complexes includes schist, paragneiss, orthogneiss, amphibolite, marble, calcium silicate rock, migmatite and granulite rocks (Kohn MJ, 2014; Wang JM et al., 2022). The exhumation of the GHC from the middle–lower crust to the near-surface occurred during the Cenozoic (Webb AAG et al., 2017). The LHS is mainly composed of Proterozoic and a small amount of Paleozoic–Mesozoic sedimentary rocks and magmatic rocks with a low degree of metamorphism, and they exhibit greenschist to amphibolite facies (Martin AJ, 2017).

The Himalayan magmatic rocks mainly date to the Paleoproterozoic (1900–1700 Ma; Imayama T et al., 2019), Neoproterozoic (1000–800 Ma; Zhang Z et al., 2021), early Paleozoic (520–460 Ma; Zhang LK et al., 2019), Permian (290–260 Ma; Tian YH et al., 2021), Late Triassic (240–210 Ma; Huang Y et al., 2018), Late Jurassic–Early Cretaceous (150–120 Ma; Chen SS et al., 2021) and Cenozoic (45–1 Ma; Burg JP and Bouilhol P, 2019). Among them, the Proterozoic and early Paleozoic magmatic rocks have generally experienced moderate to high degrees of metamorphism, forming an orthogneiss that mainly crops out in the LHS and GHC. The late Paleozoic and Mesozoic magmatic rocks are mainly distributed in the THS. The Permian and Triassic

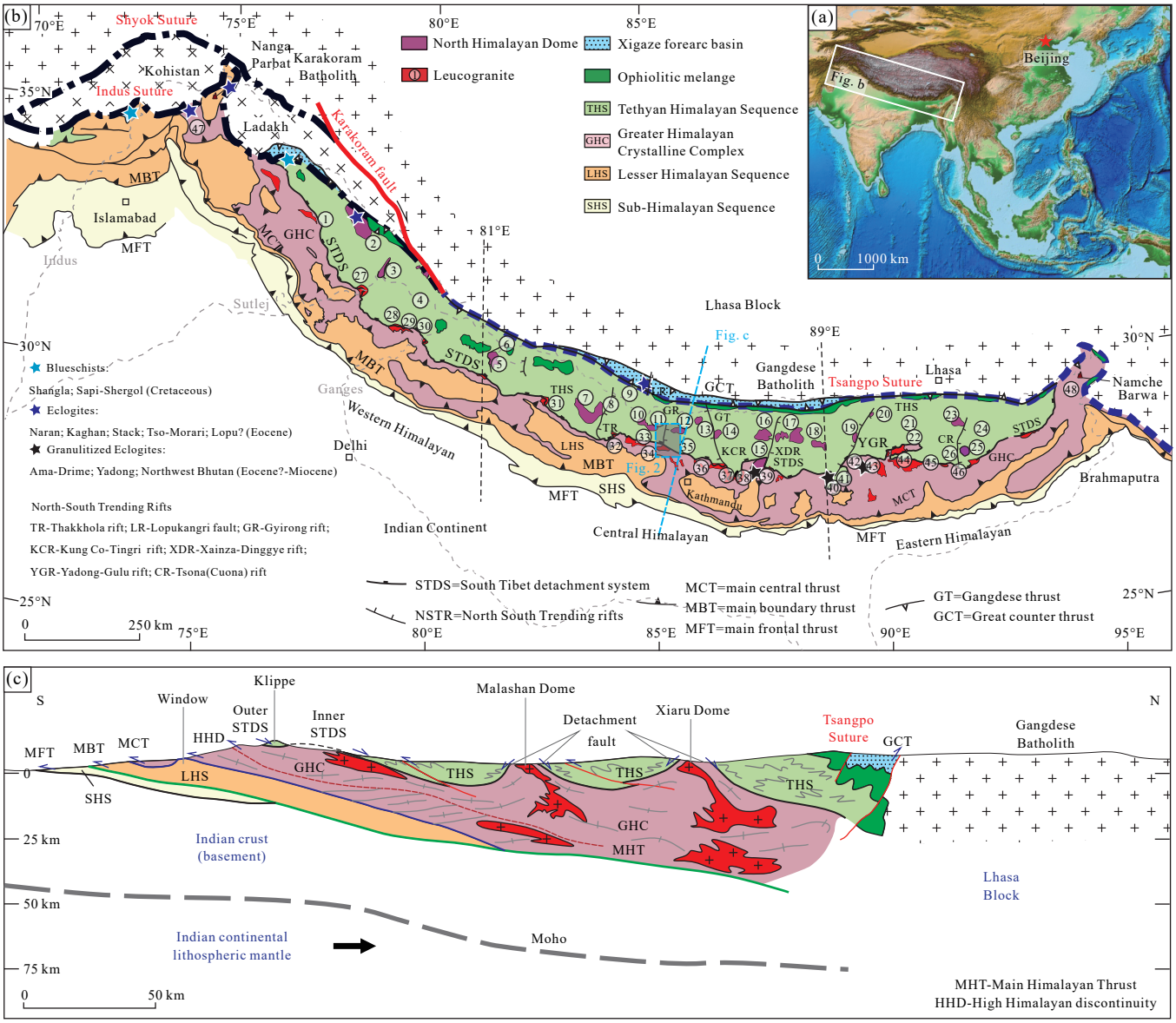

Fig. 1. Geological framework and distribution of Cenozoic granites in the Himalayas (modified from Cao HW et al. , 2022a). a–Geographical location of the study area; b–distribution map of leucogranites and gneiss domes (NHGDs) in the Himalayan region; c–geological profile of the eastern Himalayas. Gneiss domes and Cenozoic granites in the Tethyan Himalayas: 1. Zanskar (Gianbul–Gumburanjun), 2. Tso Morari, 3. Leo Pargil, 4. Zhada 5. Grula Mandhata–Xiao Gurla, 6. Mayum, 7. Mustang–Dlou–Mugu, 8. Qukangyi, 9. Niuku, 10. Changguo, 11. Qiazuweng–Kung Tang, 12. Cuobu–Malashan–Paiku, 13. Xiaru, 14. Suozuo–Dingri–Zharishizhong, 15. Dinggye–Ama Drime, 16. Lhagoi Kangri, 17. Mabja–Sakya–Kuday, 18. Kangpa, 19. Kangma, 20. Ramba, 21. Langkazi–Zhegu–Haweng–Cuomei, 22. Luozha–Lalong, 23. Yalaxiangbo–Dala, 24. Longzi–Liemai–Ridang–Quedang, 25. Cuonadong, 26. Kongbugang; Cenozoic granites in the Greater Himalayas: 27. Sutlej, 28. Garhwal–Gangotri, 29. Shivling, 30. Malari, 31. Bura Buri, 32. Dhaulagili–Annapurna–Thakkhola, 33. Manaslu, 34. Gyirong–Langtang, 35. Shisha Pangma, 36. Nyalam, 37. Qomolangma–Lhotse–Rongbuk–Pushila–Qiongjiagang, 38. Makalu, 39. Kanchenjunga–Sikkim, 40. Yadong–Dingga–Gaowu, 41. Lingshi–Jomolhari, 42. Wagya La–Chongba, 43. Masang Kang–Paro, 44. Kula Kangri–Luozha–Lalong, 45. Lakang–Kuju, 46. Cuona–Yamarong–Lebugou–Tawang, 47. western Himalayan syntaxis–Nanga Parbat, 48. eastern Himalayan syntaxis–Namcha Barwa.

magmatic rocks represent the opening of the Middle-Tethys Ocean and the Neo-Tethys Ocean, respectively (Shellnutt JG, 2018; Lin C et al., 2020). The Late Jurassic–Early Cretaceous Cuomei Large Igneous Province (LIP) is related to the Kerguelen mantle plume (Zhu DC et al., 2009), indicating that the Indian Plate and the Australian Plate began to rift, the Indian Plate drifted northwards after the breakup, and the Neo-Tethys Ocean gradually shrank and closed in the early Eocene (Yang T et al., 2015).

During the late Paleocene to early Eocene (55 ± 5 Ma), the Neo-Tethys oceanic crust was completely subducted below the Lhasa plate, marking the continent-continent collision between the Indian plate and the Lhasa plate (Hu XM et al., 2016; Searle MP and Treloar PJ, 2019; Ding H et al., 2022). Subsequently, continuous northwards subduction of Indian continental crust below the Lhasa plate occurred. The Himalayan leucogranite is divided into two zones: the northern zone is mainly exposed in the THS and in gneiss domes (Ma ZN et al., 2022), and the southern zone is mainly exposed at the top of the GHC and in the eastern and western

Himalayan syntaxes (Liu L et al., 2022). The northern and southern zones are dominated by two–mica granite and garnet–tourmaline-bearing muscovite granite, while Eocene and Miocene intermediate–basic dikes and adakitic rocks are mainly observed in the northern zone (Cao HW et al., 2020a; Fig. 1). The Cenozoic magmatism can be divided into five stages: 49–40 Ma, 39–29 Ma, 28–15 Ma, 14–7 Ma, and 6–0.7 Ma, which are mainly related to the break-off of the Neo-Tethys oceanic crust, low-angle subduction, break-off or retreat of the crustal slab of Indian continental crust, north-south-trending tearing, and the rapid uplift of the eastern and western Himalayan syntaxes, respectively (Cao HW et al., 2022a). The Himalayan leucogranite originates from the disequilibrium partial melting of the GHC and has experienced highly differentiated evolution involving mineral separation and crystallization (Ayres M and Harris N, 1997; Harris N and Ayres M, 1998). The leucogranite is characterized by high Si, K, Al, and Na contents and low Ca, Fe, Mg, Ti, Mn, and total REE contents, with significant negative Eu anomalies. The leucogranite is also characterized by high Rb/Sr and Y/Ho values and low Th/U, Nb/Ta, Zr/Hf, and K/Rb values (Cao HW et al., 2022a). With improvements in the degree of exploration, the Himalayan Cenozoic leucogranite-pegmatite belt is expected to become a new world-class Li-Be-Sn-W-Ta rare metal metallogenic belt (Cao HW et al., 2020b, 2021; Zhang ZM et al., 2022).

3. Samples and analytical methods

In this study, seven pegmatite samples were collected north of the Gyirong town (Fig. 2; GPS coordinates: E85°18'33.7", N28°24'37.7"; Pei QM et al., 2023). The surrounding rock of pegmatite is orthogneiss, and the pegmatite form is saclike. The boundary between the pegmatite and surrounding rock is blurry. The essential minerals of pegmatite include plagioclase, potassium feldspar, quartz, garnet, tourmaline, muscovite and small amounts of zircon, monazite and xenotime (Fig. 3). The diameter of the mineral grains of the Gyirong pegmatite, especially albite and tourmaline, can reach 3–4 cm, and the distribution of minerals such as garnet and tourmaline is also uneven and often shows concentrated distributions (Fig. 3).

Sample JL-1 was used for in situ U–Pb dating of zircon, monazite and xenotime, Ar-Ar dating of muscovite, and Lu-Hf isotope analysis of zircon. The other six samples were used for analysis of the major elements, trace elements and Sr-Nd-Pb isotopes of the whole rock. U–Pb dating and trace element analyses of zircon and monazite, as well as Lu–Hf isotopes of zircon, were completed by Wuhan Sample Solution Analytical Technology Co., Ltd., Wuhan, China. U–Pb dating and trace element analyses of xenotime were conducted at the State Key Laboratory of Geological Processes and Mineral Resources, China University of Geosciences, Wuhan. Muscovite Ar–Ar dating and whole-rock geochemical analyses of the pegmatite were conducted at the Beijing Research Institute of Uranium Geology.

3.1. U–Pb dating of zircon, monazite and xenotime analyses

Based on cathodoluminescence (CL) images of zircon and backscattered electron (BSE) images of monazite and xenotime, zircon, monazite and xenotime grains without obvious cracks and inclusions were selected for U-Th-Pb dating. Experiments were performed on an Agilent 7900 ICP-MS instrument (Agilent Technology, Tokyo, Japan) equipped with an ArF excimer laser (λ=193 nm) (GeoLas HD, MicroLas Göttingen, Germany). The laser ablation system featured a signal-smoothing device for improved stability of the signal and precision of the isotope ratio (Hu Z et al., 2015). Helium was used as the carrier gas in the ablation cell and mixed with argon (makeup gas) behind the ablation cell (Luo T et al., 2018). A signal-smoothing and mercury-removing device was used in this laser ablation system to obtain smooth signals and reduce the mercury signal (Hu Z et al., 2015). A small amount (4.1 mg min^{-1}) of water vapor was added before the ablation cell to improve the analytical accuracy and precision of the U-Th-Pb ages (Luo T et al., 2018, 2020). The spot diameter, frequency and energy of the laser were set as 24 μm, 5 Hz and 80 mJ, respectively, for zircon U–Pb dating. The standard material 91500 (1062 ± 4 Ma, Wiedenbeck M et al., 2004) was analyzed as an external standard. GJ-1 (608.5 ± 0.4 Ma, Jackson SE et al., 2004) and Plešovice (337.1 ± 0.4 Ma, Sláma J et al., 2008) were analyzed as unknowns at regular intervals during analysis to monitor instrumental drift. For monazite U–Pb dating, the spot diameter, frequency and energy of the laser were set as 16 μm, 2 Hz and 80 mJ, respectively. The standard material 44069 (424.9 ± 0.4 Ma, Aleinikoff JN et al., 2006) was analyzed as the external standard. Trebilcock (272 ± 4 Ma, Tomascak PB et al., 1996) was analyzed as an unknown. For xenotime U–Pb dating, the spot diameter, frequency and energy of the laser were set as 16 μm, 2 Hz and 80 mJ, respectively. The standard material 91500 (1062 ± 4 Ma, Wiedenbeck M et al., 2004) was analyzed as the external standard. BS-1 (508.9 ± 0.3 Ma, Fletcher IR et al., 2004) and MG-1 (490.0 ± 0.3 Ma, (Fletcher IR et al., 2004) were analyzed as unknowns. The measured ages of the zircon (91500, GJ-1 and Plešovice), monazite (44069 and Trebilcock) and xenotime (BS-1 and MG-1) standards showed excellent agreement with their respective reference values (Luo T et al., 2020). The trace element compositions of the minerals were calibrated against NIST 610 glass as an external calibration. Off-line selection and integration of background and analysis signals, time-drift correction, and quantitative calibration for the U-Th-Pb ages and trace element contents were performed by ICPMSDataCal (Liu Y et al., 2010). The U-Th-Pb age concordia diagram and weighted average age of the samples were calculated by IsoplotR software (Vermeesch P, 2018).

3.2. Zircon Lu-Hf isotopic analyses

Zircon Lu-Hf isotope analyses were carried out close to or in the same domain as the U–Pb dating points. The LA-MC-ICP-MS consisted of a GeoLas HD (Coherent, Germany) laser ablation system and a Neptune Plus (Thermo Fisher

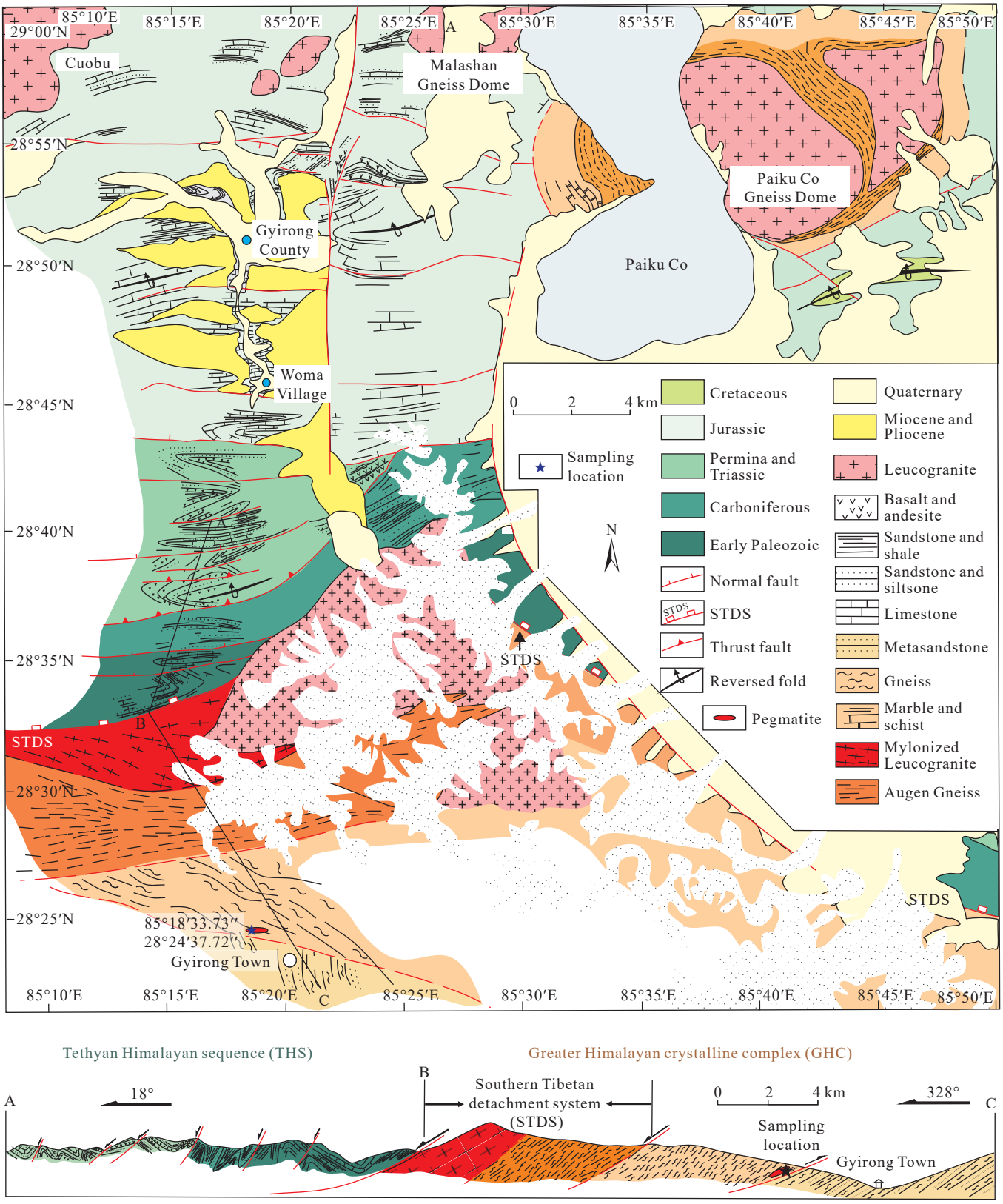

Fig. 2. Tectonic setting (a) and geological section (b) of the Gyirong area showing the sampling location (modified from Wang XX et al., 2017).

Scientific, US) MC-ICP-MS. A signal smoothing device was used to improve the stability of the signal and precision of the isotope ratio (Hu Z et al., 2015). Helium was used as the carrier gas, and a small amount of nitrogen was introduced after the ablation tank to improve the sensitivity to Hf isotopes. The high-performance cone combination designed by Neptune Plus was adopted. The laser output energy density was ~ 7.0 J/cm^2. Single point ablation mode was adopted, and the spot bundle was fixed at 44 μm. For detailed operating conditions and analytical methods, refer to Hu Z et al. (2012).

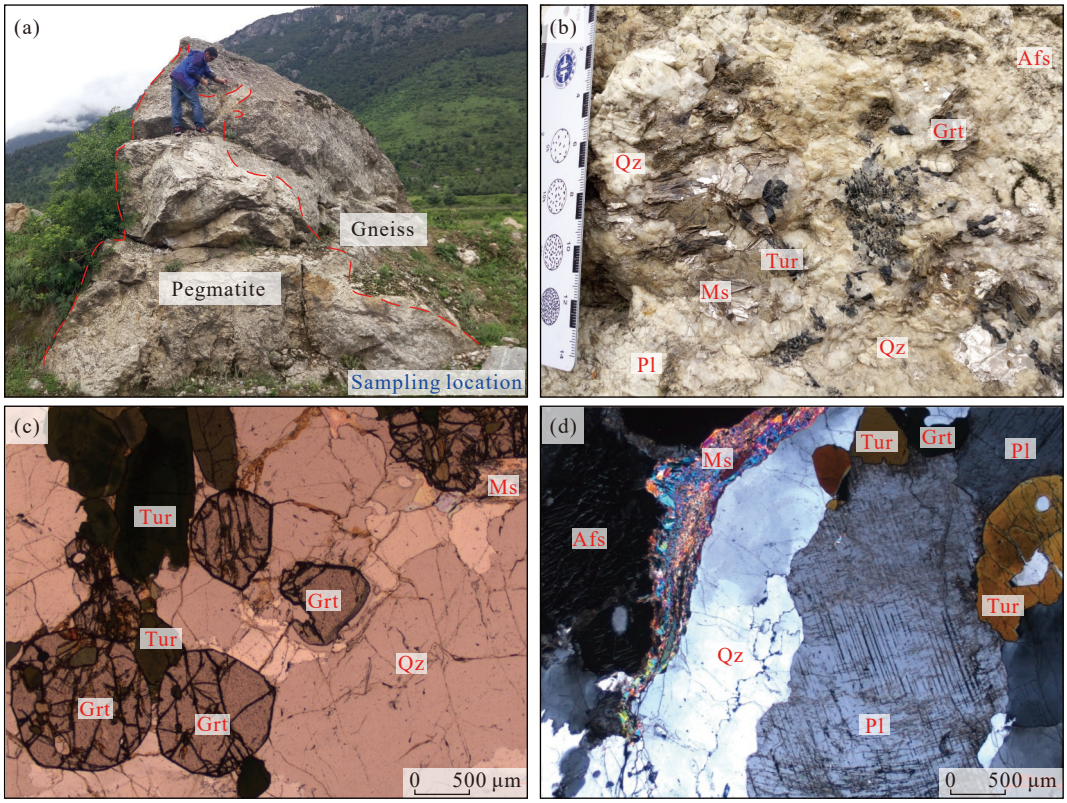

Fig. 3. The field outcrop (a), hand specimen photographs (b) and photomicrographs (c and d) show the petrological characteristics of the pegmatite in the Gyirong town. The main minerals are quartz (Qz), alkali feldspar (Afs), plagioclase (Pl), muscovite (Ms), tourmaline (Tur) and garnet (Grt).

The standard material 91500 ($^{176}Hf/^{177}Hf$=0.282293 ± 28, Woodhead J et al., 2004) was analyzed to create the calibration curve as an external standard. GJ-1 (0.282000 ± 5, Morel MLA et al., 2008) and Temora (0.282686 ± 14, Woodhead J et al., 2004) were analyzed as the check standards. Off-line processing of analytical data was completed by ICP-MS DataCal software (Liu Y et al., 2010).

3.3. Muscovite Ar-Ar dating analyses

Muscovite samples were ground to 40–60 mesh powder. After cleaning and drying, appropriate amounts (10–20 mg) of muscovite samples and standard sample ZBH-25 were separately packed with aluminum foil and sealed in quartz tubes. Then, the samples were irradiated by the B4 channel in a fast neutron reactor for 24 hours at the China Institute of Atomic Energy. The integrated neutron flux was 2.65×10^{13} n $cm^2\cdot s^{-1}$. The irradiated samples underwent step-heating (temperature ranged from 600 to 1420 °C) to extract gas after 1–2 months. The released gas was purified by zirconium–aluminum pump adsorption. The ratio of $^{40}Ar^*/^{39}Ar$ ($^{40}Ar^*$ indicates radiogenic argon) in the argon released in each temperature step was analyzed. The Ar isotopes were analyzed by a Helix SFT Inert Gas Mass Spectrometer (Thermo Fisher Scientific, US). The age of the biotite standard sample ZBH-25 is 133.1±1.3 Ma (Sang HQ et al., 2006), with K=7.599% and $^{40}Ar=1.8157\times10^{-9}$ (mol/g). The analytical data were calibrated by mass discrimination, atmospheric argon correction, blank correction, and coefficient correction. The correction coefficients of interference isotopes produced during neutron irradiation were obtained by analyzing the radiogenic K_2SO_4 and CaF_2. The age spectrum was drawn by using ArArCALC ver2.4 software (Koppers AAP, 2002) to calculate the age and the cumulative percentage of ^{39}Ar in each temperature range. The plateau age was calculated by the weighted method. The initial $^{40}Ar/^{39}Ar$ ratio and isochron age were calculated by the linear fitting method (Ludwig KR, 2012).

3.4. Whole-rock major and trace elements chemical analyses

Whole-rock major element analyses were conducted on an XRF instrument (Primus II, Rigaku, Japan). The detailed sample digestion procedure was as follows: (1) Sample powder (200 mesh) was placed in an oven at 105 °C to dry for 12 hours. (2) Approximately 1.0 g of dried sample was accurately weighed, placed in a ceramic crucible and then heated in a muffle furnace at 1000 °C for 2 hours. After cooling to 400 °C, the sample was placed in a drying vessel and weighed again to calculate the loss on ignition (LOI). (3) The sample powder (0.6 g) was mixed with 6.0 g cosolvent ($Li_2B_4O_7$: $LiBO_2$: LiF=9 : 2 : 1) and 0.3 g oxidant (NH_4NO_3) in a Pt crucible and placed in the furnace at 1150 °C for 14 min. Then, the molten sample was quenched with air for 1 min to produce flat discs on a fire brick for XRF analyses.

Whole-rock trace element analyses were conducted on an Agilent 7700e ICP-MS. The detailed sample digestion

procedure was as follows: (1) Sample powder (200 mesh) was placed in an oven at 105 °C to dry for 12 hours; (2) 50 mg of sample powder was accurately weighed and placed in a Teflon bomb; (3) 1 mL HNO_3 and 1 mL HF were slowly added to the Teflon bomb; (4) the Teflon bomb was put into a stainless steel pressure jacket and heated to 190 °C in an oven for >24 hours; (5) after cooling, the Teflon bomb was opened and placed on a hotplate at 140 °C and evaporated to incipient dryness, and then 1 mL HNO_3 was added and evaporated to dryness again; (6) 1 mL of HNO_3, 1 mL of MQ water and 1 mL internal standard solution of 1×10^{-6} In were added, and the Teflon bomb was resealed and placed in the oven at 190 °C for >12 hours; and (7) the final solution was transferred to a polyethylene bottle and diluted to 100 g by the addition of 2% HNO_3. The analytical precision and accuracy for whole-rock major elements are better than 2% and 5% by XRF, and those for whole-rock trace elements are better than 5% and 10% by ICP-MS.

3.5. Whole-rock Sr-Nd-Pb isotopic analyses

Whole-rock Sr-Nd-Pb isotope analysis was performed using a Thermo Fisher Scientific MC-ICP-MS (Neptune Plus) instrument. During Sr isotope analysis, seven samples were inserted between two standard samples (NBS SRM 987 and AlfaSr) for analysis. The analytical accuracy (2SE) was 0.000010–0.000020 (0.01‰–0.03‰, 2RSE), and the accuracy was better than 0.000020 (about 0.03‰). During Nd isotope analysis, seven samples were inserted between two standard samples (JNDI-1 and AlfaNd). The analytical accuracy (2SE) was 0.000005–0.000025 (0.01 ‰ –0.05 ‰, 2RSE), and the accuracy was better than 0.000025 (about 0.05 ‰). The accuracies of $^{206}Pb/^{204}Pb$, $^{207}Pb/^{204}Pb$ and $^{208}Pb/^{204}Pb$ were 0.002%–0.025% (2RSE), which were better than 0.03%. BCR-2 (basalt) and RGM-2 (rhyolite) were used as monitoring samples for the Sr, Nd and Pb isotope analyses. The standard sample and monitoring sample results were consistent with the recommended values within the error range.

4. Results

4.1. U–Pb ages of zircon, monazite and xenotime

The zircons of the Gyirong pegmatite are mostly long columnar with a size of approximately 80–250 μm. Some of the zircons in the CL image have a clear core–mantle–rim structure. The core and mantle domains are rounded, light in color, and have obvious zonal structures, indicating that these domains are inherited zircons. The rim domains are dark in color, grayish-black, lacking zonal structure and displaying an obvious foam-like texture, which are typical characteristics of anatectic zircons (Corfu F et al., 2003; Fig. 4a). In total, 78 zircon spots for U–Pb isotopes were dated in this study, and 46 points were located on rims (Supplementary Table 1). The $^{206}Pb/^{238}U$ and $^{207}Pb/^{235}U$ ages showed good consistency (> 90%) (Fig. 5a). The average Th and U contents of the inherited zircon material are 135.7×10^{-6} and 888.0×10^{-6}, respectively. In contrast, the Th and U contents of the Cenozoic anatectic zircon material are much higher, with average contents of 424.4×10^{-6} and 7939.5×10^{-6}, respectively. Himalayan Cenozoic granite usually has high Th and U contents with large variations. This may be related to its metamorphic process (Zeng LS et al., 2015). The average Th/U values of the inherited zircon and anatectic zircon are 0.28 and 0.04, respectively. Except for a small number of Proterozoic zircons, the inherited zircon ages in the core–mantle region are mainly concentrated in the early Paleozoic (480–460 Ma), while the ages of the zircon material in the rim are relatively dispersed and continuous, ranging from 36.8 to 21.6 Ma with a peak value of 29 Ma (Figs. 5b and 5c). The eight youngest zircon ages are concentrated in the range of 24.6–21.6 Ma, with a weighted average of 22.4±0.7 Ma (MSWD=2.1).

The monazite grains are grayish white, subhedral, and show columnar or granular features with a size range of 100–150 μm (Fig. 4b). The BSE photograph illustrates that few zoning textures are present, and core–rim textures are lacking. In this study, the monazite U–Pb isotopes were measured at 30 points (Supplementary Table 2). The $^{206}Pb/^{238}U$ and $^{207}Pb/^{235}U$ ages showed good consistency, which was greater than 90% (Fig. 5d). Consistent with the age characteristics of the abovementioned anatectic zircons, the monazite ages are continuously distributed between 33.6 and 23.4 Ma (Fig. 5e), with a peak value at 30 Ma (Fig. 5f). The two youngest ages from the monazite grains are 23.7 Ma and 23.4 Ma, with a weighted average of 23.5±0.4 Ma (MSWD= 0.4), which is close to the youngest zircon U–Pb age.

The xenotime grains are bright white in color and display short columnar and granular features, and their size range is 80–120 μm in length. As shown in the BSE images (Fig. 4c), the characteristics of the mineral fabrics are similar to those of monazite. The results of the U–Pb isotope analyses of 50 xenotime grains are listed in Supplementary Table 3. Except for 8 points, the $^{206}Pb/^{238}U$ and $^{207}Pb/^{235}U$ ages of the remaining 42 points have high concordance, which is greater than 90% (Fig. 5g). Except for one spot with an age of 254.4 Ma, the remaining ages are Cenozoic. The xenotime grains show continuously distributed ages ranging from 38.6 to 16.1 Ma (Fig. 5h), with a peak value at 25 Ma (Fig. 5i), which coincides with the age characteristics of the anatectic zircons and monazites. The four youngest ages are concentrated in the range of 16.1–16.9 Ma, with a weighted average of 16.5±0.3 Ma (MSWD = 1.6), which is far younger than the youngest U–Pb age of the abovementioned zircons and monazites.

The REEs and trace elements of zircon, monazite, and xenotime are quite different, and there is no clear correspondence between the contents of REEs, trace elements and ages (Fig. 4d). The anatectic zircons display relatively low total amounts of rare earth elements (ΣREEs) (mean=2512×10^{-6}) and are enriched in heavy REEs (HREEs). The average Ti content of Cenozoic anatectic zircons is 5.9×10^{-6} and yields low Ti-in-zircon temperatures with an

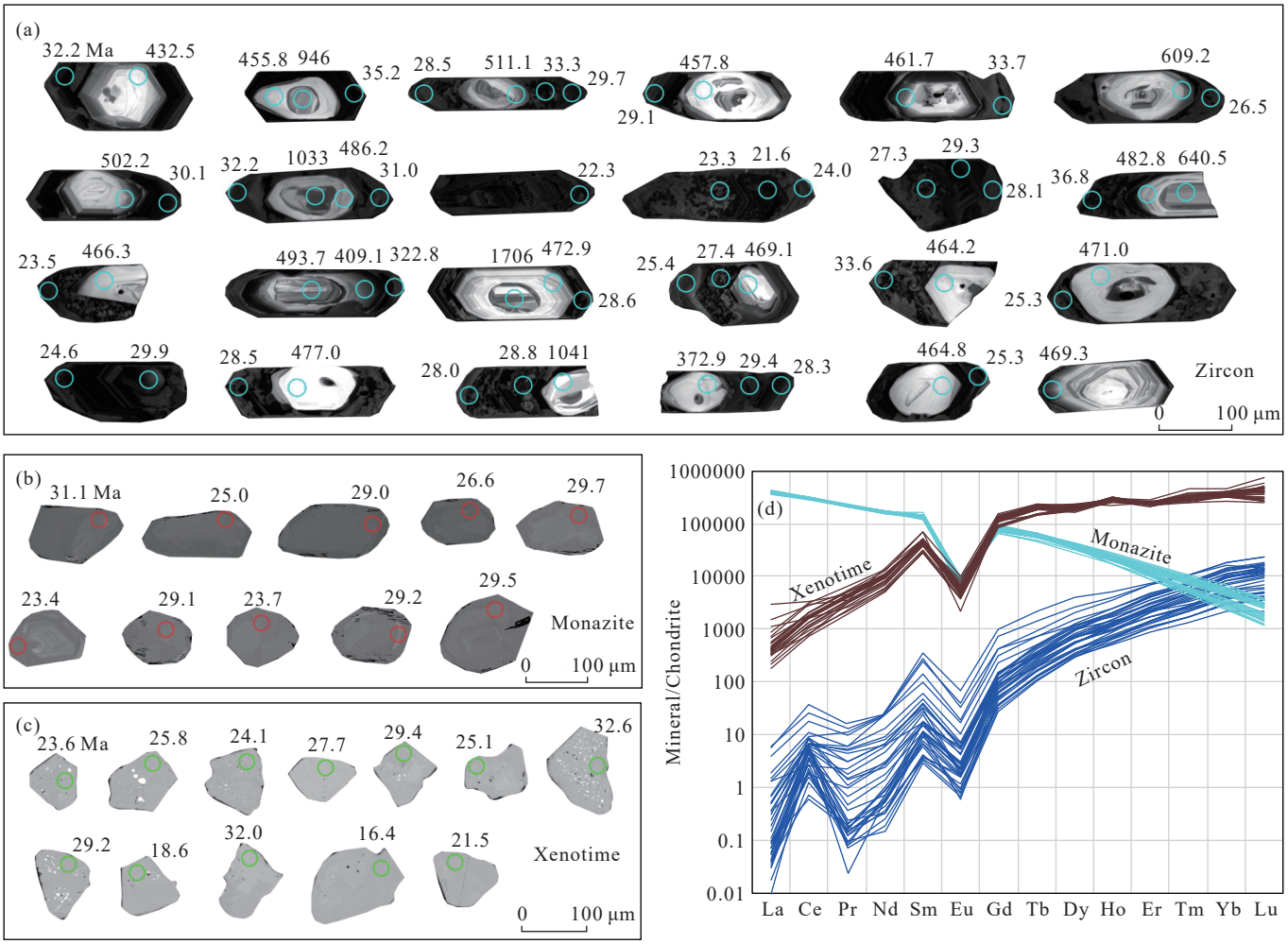

Fig. 4. Cathodoluminescence (CL) images of zircons (a), backscattered electron (BSE) images of monazite (b) and xenotime (c) showing the dating position and ages. Normalized rare earth element compositions of zircon, monazite and xenotime (e). Chondrite meteorite values are quoted from Sun SS and McDonough WF (1989).

average of 688°C (Ferry JM and Watson EB, 2007). The zircons show low Lu contents (mean=255×10^{-6}) and high Hf contents (mean=19504×10^{-6}) with an average Lu/Hf ratio of 0.01. The xenotime contains abundant REEs with an average ΣREE of 231823×10^{-6} and is especially enriched in HREEs. The monazite has the highest ΣREE (mean=430199×10^{-6}), but it is enriched in light REEs (LREEs).

4.2. Zircon Lu-Hf isotope geochemistry

In situ Lu-Hf isotope analysis was performed at the locations of zircon U–Pb isotope laser analysis spots. In this study, a total of 45 points were analyzed, of which 20 points were within the inherited zircon in the core and the mantle, and 25 points were located at the rim (Supplementary Table 4). The average value of $f_{Lu/Hf}$ of zircon is −0.9, and the $^{176}Lu/^{177}Hf$ ratio shows a low average value of 0.0019, indicating that ^{177}Hf was formed by the decay of ^{176}Lu. Thus, the $^{176}Hf/^{177}Hf$ ratio obtained from this study represents the isotope ratio at the time of its formation (Wu FY et al., 2007). The $\varepsilon_{Hf}(t)$ values of inherited zircons vary greatly, ranging from −12.7 to 3, with a mean of −7.1 (Fig. 6a). The average two-stage model (T_{DM2}) age is 1.82 Ga (Fig. 6b). In contrast, the Cenozoic anatectic zircons display a narrow range of $\varepsilon_{Hf}(t)$ concentrations between −12 and −9 (mean=−11.4) with an average T_{DM2} age of 1.60 Ga, which indicates that the Gyirong pegmatite has a homogeneous magma source (Fig. 6c).

4.3. Muscovite Ar–Ar age

The ^{40}Ar-^{39}Ar analytical results for muscovite from the pegmatite in Gyirong are illustrated in Fig. 7 and listed in Supplementary Table 5. Muscovite from the pegmatite yields a ^{40}Ar-^{39}Ar plateau age of 16.1 ± 0.2 Ma (MSWD = 5.1) based on 99.77% of the released ^{39}Ar, which was calculated from steps 1–8 (Fig. 7a). The inverse isochron age is 15.2 ± 0.4 Ma (MSWD = 2.4) with an intercept on the $^{40}Ar/^{36}Ar$ axis of 327±12 corresponding to the composition of atmospheric argon (Fig. 7b), which is concordant with the plateau age within the margin of error. The age of muscovite is slightly younger than the U–Pb ages of zircon, monazite and xenotime (Fig. 8).

4.4. Whole-rock major and trace elements geochemistry

The Gyirong pegmatite shows high SiO_2 in a range

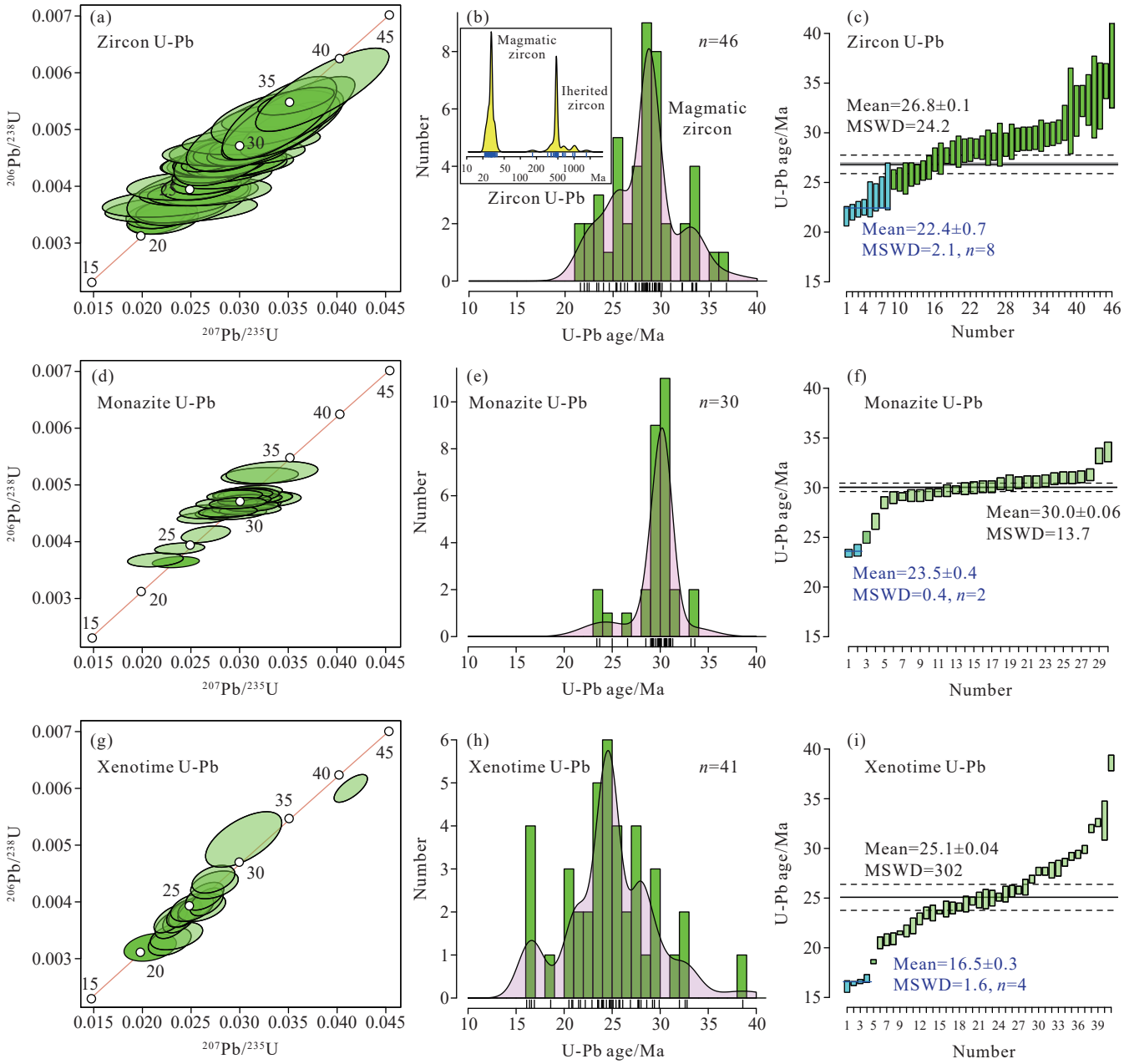

Fig. 5. Zircon, monazite and xenotime U-Th-Pb geochronology of the Gyirong pegmatite. Zircon U–Pb concordia diagrams (a), kernel density estimates (KDEs) showing age frequency distribution (b), and the weighted mean ages (c). Monazite U–Pb concordia diagrams (d), KDEs (e), and the weighted mean ages (f). Xenotime U–Pb concordia diagrams (g), KDEs (h), and the weighted mean ages (i).

between 66.08 and 75.65% and nearly consistent Al_2O_3 varying from 13.78% to 18.34%, with means of 72.22% and 15.61%, respectively. They show relatively high K_2O (mean=7.13%) contents and low Na_2O (mean=2.71%), CaO (mean=0.94%) and $Fe_2O_3^{Total}$ (mean=0.52%) contents. Due to the high K_2O contents with large variations, the Na_2O+K_2O–CaO value varied significantly between 5.05 and 14.14 (Fig. 9a). The A values (Al–(K+Na+2Ca)) and B values (Fe+Mg+Ti) of the Gyirong pegmatite are 16–48 and 2–16, respectively, which indicate that there are few dark minerals with a peraluminous composition (Fig. 9b; Debon F and Le Fort P, 1983, 1988). Similarly, the Gyirong pegmatite shows a high aluminum saturation index, with A/CNK ($(Al_2O_3/(Na_2O+K_2O+CaO)_{\text{molar ratio}}$) values between 1.04 and 1.22, A/NK ($(Al_2O_3/(Na_2O+K_2O)_{\text{molar ratio}}$) values between 1.1 and 2.0 and a total alkali content (K_2O+Na_2O) between 1.09 and 1.58 (Fig. 9c). The contents of FeO^{Total}, MnO, P_2O_5, MgO, and TiO_2 in the pegmatite are all extremely low, and the average values are 0.37%, 0.06%, 0.04%, 0.17%, and 0.04%, respectively.

The relatively low ΣREEs with large variations (especially for HREEs) in the Gyirong pegmatite (Fig. 10a, Supplementary Table 6) may be due to the large size of the pegmatite mineral crystals and the uneven distribution of minerals (Fig. 3). The ΣREEs contents are between 19.33×10^{-6} and 66.97×10^{-6}, with an average of 43.64×10^{-6}. The Gyirong pegmatite shows no Ce anomalies but significant Eu anomalies with δEu values ranging from 0.86 to 2.55

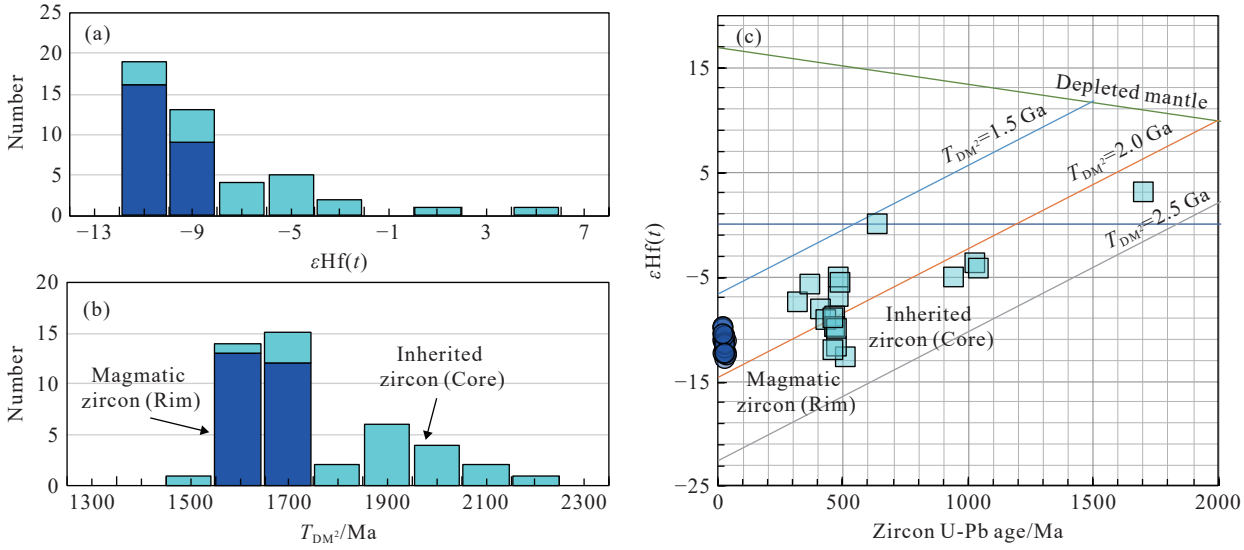

Fig. 6. Histograms of the zircon $\varepsilon_{Hf}(t)$ (a) and two–stage model age results (b). Scatter plot of the zircon U–Pb age *versus* $\varepsilon_{Hf}(t)$ (c).

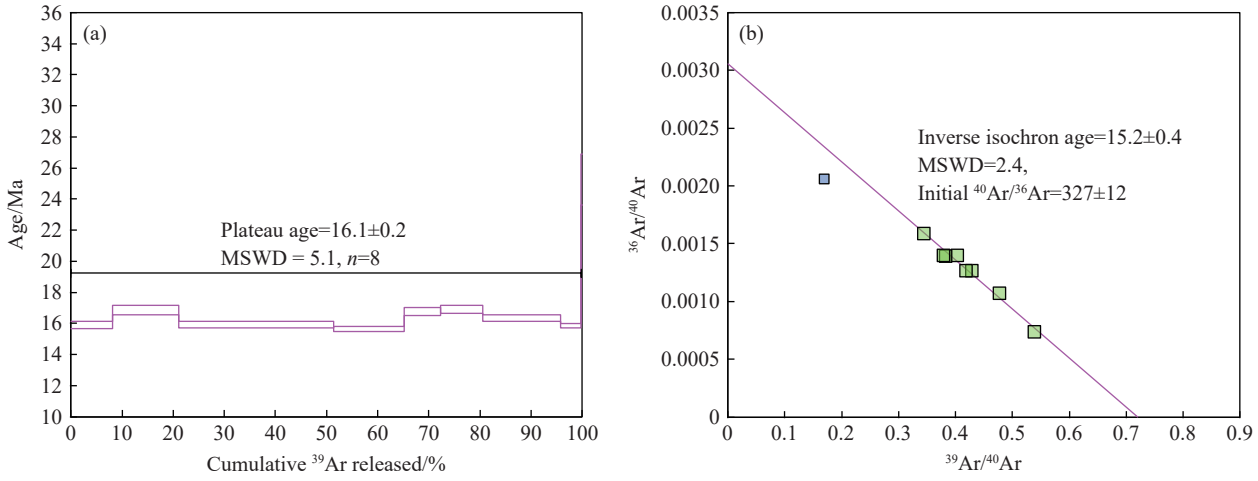

Fig. 7. ^{40}Ar-^{39}Ar plateau age of muscovite from the Gyirong pegmatite (a). Isochron Ar-Ar age of muscovite (b).

(mean=1.45). The $TE_{1,3}$ (tetrad effect of REEs, Irber W, 1999) values of the Gyirong pegmatite are in the range of 1.02–1.12 (generally < 1.1), indicating no significant tetrad effect. The average Rb and Sr values of the pegmatite are 336×10^{-6} and 86×10^{-6}, respectively, and the average Rb/Sr value is 3.7. The average Y value is 16.72×10^{-6}, and the Sr/Y value is relatively low, with an average of 16.3×10^{-6}. Overall, the Gyirong pegmatite is enriched in Rb, Cs, U, K, Th, and Pb and depleted in Nb, Ta, Zr, Ti, Eu, Sr, Ba, etc. (Fig. 10b).

4.5. Whole-rock Sr-Nd-Pb isotopic geochemistry

The Gyirong pegmatite exhibits high Rb and Sr contents. The ratios of $^{87}Rb/^{86}Sr$ and $^{87}Sr/^{86}Sr$ are variable (Fig. 11a), with averages of 10.78 and 0.7642, respectively (Supplementary Table 6). The initial whole-rock $^{87}Sr/^{86}Sr_{(16\ Ma)}$ values range from 0.751 to 0.765, with an average of 0.762 (Fig. 11b). In contrast, the pegmatite contains relatively low Sm and Nd contents, with averages of 1.46×10^{-6} and 5.68×10^{-6}, respectively. The measured values of $^{147}Sm/^{144}Nd$ and $^{143}Nd/^{144}Nd$ show minor variations, with average values of 0.16 and 0.5118, respectively. The average initial values of $^{143}Nd/^{144}Nd_{(16\ Ma)}$ and $\varepsilon_{Nd(16\ Ma)}$ for the whole rock are 0.5118 and −16.0, respectively (Fig. 11b). The T_{DM2} ages for Nd isotopes are between 2.0 and 2.3 Ga, with an average of 2.1 Ga. The average contents of U, Th, and Pb in the Gyirong pegmatite are 10.4×10^{-6}, 8.9×10^{-6} and 75.3×10^{-6}, respectively. The Pb isotope compositions show a narrow range, and combined with the contents of U, Th and Pb, the average initial values of $^{208}Pb/^{204}Pb_{(16\ Ma)}$, $^{207}Pb/^{204}Pb_{(16\ Ma)}$ and $^{206}Pb/^{204}Pb_{(16\ Ma)}$ are 39.72, 15.79 and 19.56, respectively.

5. Discussion

5.1. Timing of the Gyirong pegmatite

The range of zircon U–Pb ages of Himalayan leucogranites is generally broad, and the $^{206}Pb/^{238}U$ ages and $^{207}Pb/^{235}U$ ages have a low degree of concordance. For example, the age range of the Khumbu Himalayan leucogranite is 48.4–15.5 Ma (Larson KP et al., 2022). The

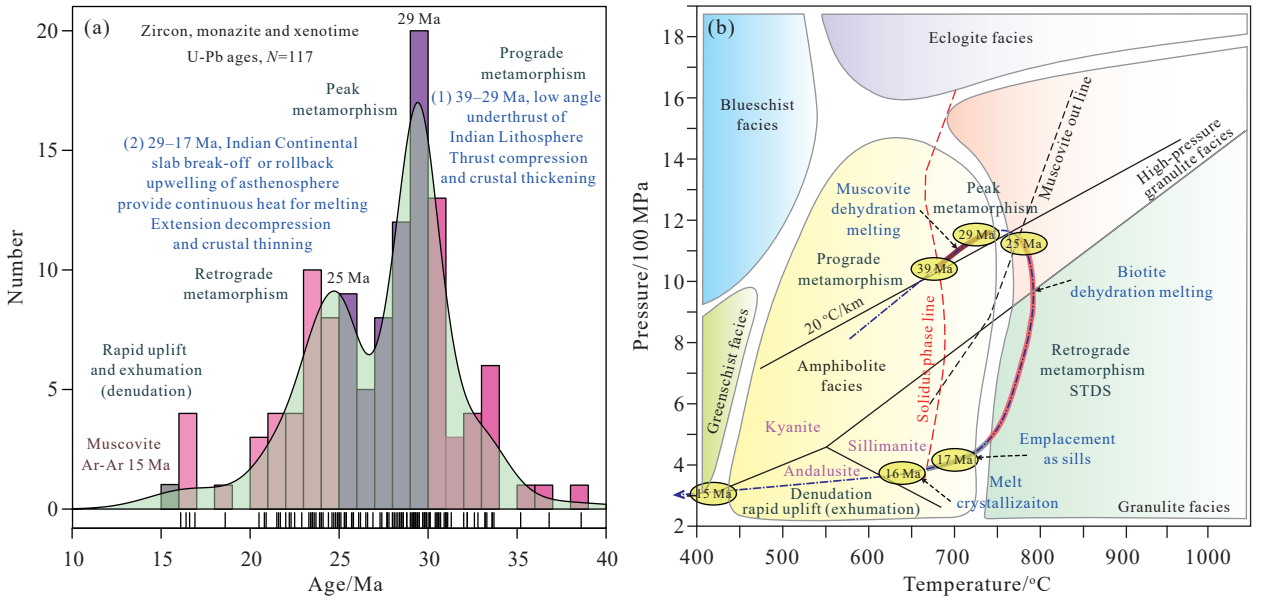

Fig. 8. Histogram of U–Pb age of zircon, monazite and xenotime and Ar-Ar age of muscovite from Gyirong pegmatite (a). Metamorphic pressure–temperature–time (P–T–*t*) path and stages of the Greater Himalayan sequence, showing the duration of muscovite and biotite dehydration and melt crystallization (b). Modified from Zhang ZM et al. (2022) and Gou ZB et al. (2022).

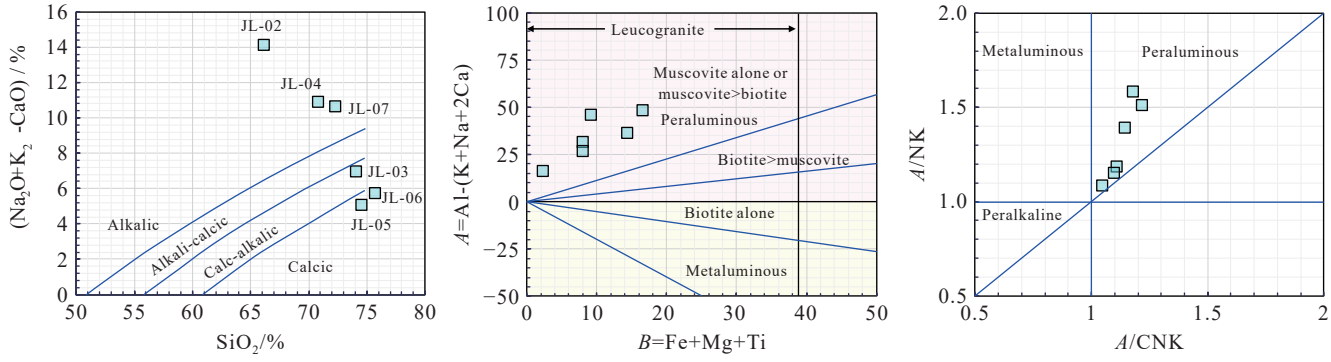

Fig. 9. Classification nomenclature diagram of SiO_2 *versus* Na_2O+K_2O–CaO (a). Modified from Frost CD and Frost BR (2011). Cationic classification of A=Al–(K+Na+2Ca) *versus* B=Fe+Mg+Ti (b). Modified from Debon F and Le Fort P (1983). Diagram of A/CNK *versus* A/NK (c). Modified from Maniar PD and Piccoli PM (1989).

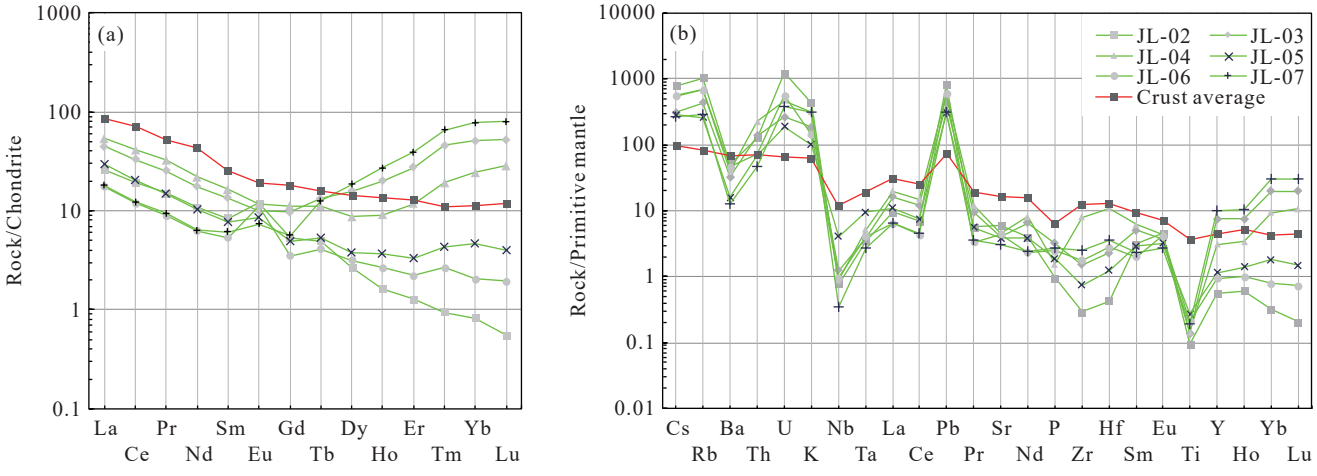

Fig. 10. Chondrite– and primitive mantle–normalized rare earth element (a) and trace element (b) spider charts for the Gyirong pegmatite. Chondrite meteorite and primitive mantle values are quoted from Sun SS and McDonough WF (1989) and McDonough WF and Sun SS (1995). The average values for the total continental crust are quoted from Rudnick RL and Gao S (2014).

age range of the Tama Kosi leucogranite is 27.5–18.0 Ma (Cottle JM et al., 2018), and the deformed leucogranites in the Ramba gneiss dome are 23.8–10.3 Ma (Chen S et al., 2022). For more examples, please refer to studies on the Nyalam

(Leloup PH et al., 2015), Leo Pargil (Lederer GW et al., 2013), Sikkim (Kellett DA et al., 2013), Bura Buri (Carosi R et al., 2013) and Cona (Liu L et al., 2022) leucogranites. Previous studies have suggested that the zircons of the Himalayan leucogranites have relatively high U contents, which limits the use of zircon U–Pb dating for some leucogranites (Wu FY et al., 2020). However, the U–Pb ages of other uranium-bearing accessory minerals (monazite, xenotime, and apatite) exhibit the same problem (Cottle J et al., 2019). This indicates that the variable age results are not due to the error caused by high U contents, but to the characteristics of the leucogranite itself (Gou ZB et al., 2016, 2019). Therefore, numerous scholars regard the youngest U–Pb age as the crystallization age of the leucogranite, and the older ages are considered to be the result of inheritance from the magma source area or xenoliths of uranium-bearing accessory minerals from the surrounding rocks (Cottle JM et al., 2018).

The U–Pb ages of the zircon, monazite, and xenotime of the Gyirong pegmatite are all variable (Fig. 5). The age results of zircon and monazite are relatively similar, and the youngest ages are concentrated at 22–23 Ma, while the xenotime ages are generally younger than the U–Pb ages of zircon and monazite, and the youngest age is concentrated at 16.5 Ma. The Pb isotope closure temperature of xenotime is close to or even higher than that of zircon (Liu ZC et al., 2011; Wu FY et al., 2015, 2020). The rocks in this study are relatively fresh and have no hydrothermal alteration. Therefore, Pb loss due to hydrothermal alteration in later periods can be ruled out. It is also difficult to explain why the Pb isotope of zircon and monazite were not affected, even if the U–Pb isotopic system of xenotime was modified by late hydrothermal activity. This study prefers to use the minimum U–Pb age of xenotime to represent the crystallization age of this pegmatite. Therefore, this study believes that the crystallization age of the Gyirong pegmatite is 16.5 Ma, and Cenozoic ages predating 16.5 Ma are metamorphic ages inherited from the partial melting source region (Zhang ZM et al., 2017).

5.2. Genesis of the Gyirong pegmatite

The mineral crystals of pegmatite are relatively large, so the results of whole-rock elemental analysis vary greatly (London D and Kontak DJ, 2012; London D and Morgan GB, 2012). In the field sampling process, this study tried its best to

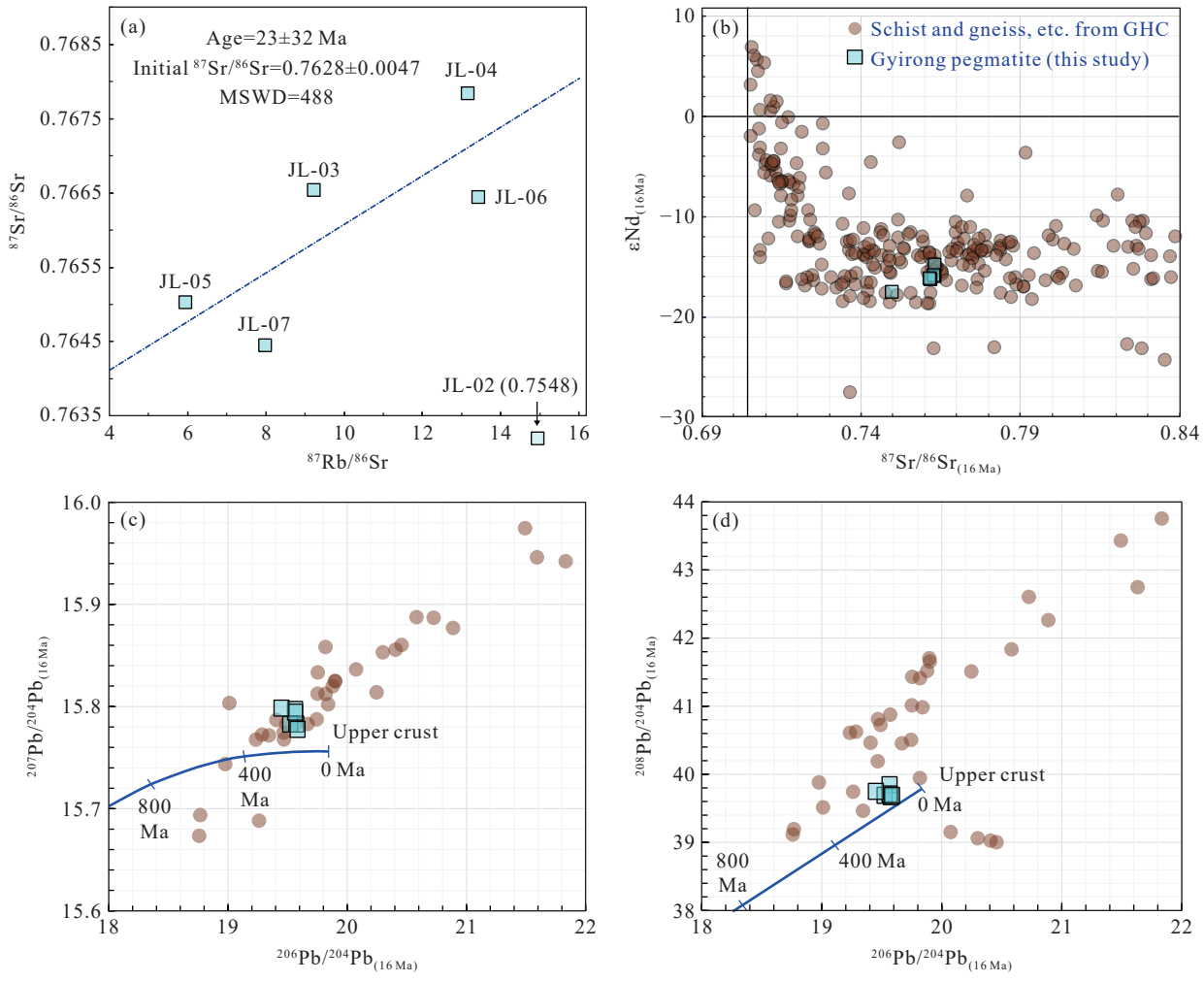

Fig. 11. Diagrams of whole–rock $^{87}Rb/^{86}Sr$ *versus* $^{87}Sr/^{86}Sr$ (a), $^{87}Sr/^{86}Sr_{25\,Ma}$ *versus* $\varepsilon_{Nd(16\,Ma)}$ (b), $^{207}Pb/^{204}Pb_{(16\,Ma)}$ *versus* $^{206}Pb/^{204}Pb_{(16\,Ma)}$ (c) and $^{208}Pb/^{204}Pb_{(16\,Ma)}$ *versus* $^{206}Pb/^{204}Pb_{(16\,Ma)}$ (d) for the Gyirong pegmatite. The Sr–Nd–Pb isotopes of GHC are from Cao HW et al. (2022a).

ensure the representativeness of each sample. Some elements in the Gyirong pegmatite vary significantly, such as SiO_2, K_2O, Eu, Zr, and HREEs (Figs. 9 and 10). It is speculated that this is mainly caused by the uneven distribution of minerals such as feldspar, garnet and zircon. However, the Sr-Nd-Pb isotopic compositions vary within a small range (Figs. 11). Therefore, the geochemical analysis results in this area are considered to be a representative case study and can reflect the geochemical properties of the pegmatite.

As previously mentioned, the Gyirong pegmatite is typically enriched in Si, Al, and Rb and depleted in Ca, Fe, Mn, P, Mg, Ti, Sr and Ba. The average Rb/Sr and Rb/Ba ratios are 3.7 and 1.6, respectively. The pegmatite displays low Nb/Ta and Th/U ratios and high K/Rb ratios. The Zr/Hf and Y/Ho ratios are similar, with average values of 24.7 and 26.7, respectively. Combined with the geochemical signatures of REEs, these features could be interpreted to indicate that the Gyirong pegmatite has not experienced a high degree of differentiation (Zeng LS and Gao LE, 2017; Wu FY et al., 2017). In addition, the Gyirong pegmatite contains a large amount of garnet, so it is characterized as a typical peraluminous S-type granite.

The anatectic zircons from the Gyirong pegmatite contain low $\varepsilon_{Hf}(t)$ values, with an average of −11.4. The whole-rock samples display high $^{87}Sr/^{86}Sr_{(16\ Ma)}$ (0.762), $^{208}Pb/^{204}Pb_{(16\ Ma)}$ (39.72), $^{207}Pb/^{204}Pb_{(16\ Ma)}$ (15.79) and $^{206}Pb/^{204}Pb_{(16\ Ma)}$ (19.6) and low $\varepsilon_{Nd(16\ Ma)}$ (−16.0) values, which are consistent with those of the GHC (Cao HW et al., 2022a, 2022b). This study identifies anatectic zircon T_{DM2}(Hf) ages of 1.60 Ga and whole-rock T_{DM2}(Nd) ages of 2.1 Ga. The Sr-Nd-Pb-Hf isotopic signatures of the Gyirong pegmatite are similar to those of the granitoids within the Gyirong area (Gao LE et al., 2017; Wang XX et al., 2017). These mineralogical, chemical and isotopic features indicate that the Gyirong pegmatite originated from the remelting of GHC crust-derived materials.

The Zr and LREE contents of the whole rock of the Gyirong pegmatite define average saturation temperatures of 626°C and 691°C, respectively (Watson EB and Harrison TM, 1983; Montel JM, 1993), which are consistent with the Ti-in-zircon temperature of 688°C (Ferry JM and Watson EB, 2007). These temperature calculation results provide mutual verification, indicating that the crystallization temperature of the Gyirong pegmatite was between 630°C and 690°C, which is close to the solid phase line temperature of metamorphic rocks (Fig. 8b). The zircon grains in the Gyirong pegmatite have a typical core-mantle-rim structure, with inconspicuous zircon zoning at the rim, a relatively dark color, extremely low Th/U values, and a wide range of age distributions (Chen RX and Zheng YF, 2017; Rubatto D, 2017). The partial melting process for Himalayan leucogranite is divided into water-present partial melting and water-absent (dehydration) partial melting (Gao LE and Zeng LS, 2014; Gao LE et al. 2017; Zeng LS and Gao LE, 2017). The Gyirong pegmatite has relatively high Rb contents and Rb/Sr ratios and low Sr and Ba contents. Furthermore, the pegmatite exhibits low Th contents (mean=8.9×10^{-6}) and high U contents (mean=10.4×10^{-6}). These geochemical characteristics are similar to the geochemical characteristics of leucogranites formed by partial melting by dehydration (Gao LE et al., 2017). The tourmalines from the Gyirong pegmatite show a tight range of $\delta^{11}B$ values between −11.8 and −9.7, and the geochemical characteristics of tourmaline also indicate that this pegmatite originated from anatexis of metapelitic rocks in the GHC (Pei QM et al., 2023). Based on the above evidence, this study suggests that the Gyirong pegmatite represents an anatectic pegmatite rather than one formed via the highly differentiated evolution of granite (Müller A et al., 2017).

5.3. Tectonic setting of the Gyirong pegmatite

The emplacement time of the two-mica granite at the top of the GHC on the northern side of the study area is 21.8–19.5 Ma (Yang XY et al., 2009; Wolff R et al., 2022). The crystallization age of the anatectic granite near the study area is 18.7 Ma (Wang XX et al., 2013). The crystallization ages of the leucogranites on the northwestern, southwestern, and southeastern sides of Gyirong town are 22.0 Ma, 17.2 Ma and 16.4 Ma, respectively (Gao LE et al., 2016). Therefore, the emplacement crystallization time of leucogranites in the Gyirong area is mainly concentrated at 22–16 Ma. However, it is worth noting that the zircon U–Pb ages of the abovementioned Gyirong leucogranites all have a wide distribution range. For example, the zircon U–Pb age of the two-mica granite at the top of the GHC is 37.6–19.3 Ma (Yang XY et al., 2009). The zircon U–Pb ages of the anatectic granite near the study area are 26.8–18.2 Ma (Wang XX et al., 2013).

Previous studies also suggest that the GHC has experienced a long period of extensive metamorphosis. The GHC metamorphism age of Namcha Barwa in the eastern Himalayan syntaxis is 42–13 Ma (Zhang ZM et al., 2015; Kang D et al., 2020; Ding H et al., 2021; Zhang ZM et al., 2022). The metamorphic age of the Yadong region in the middle section of the Himalayas is 30–13 Ma (Zhang ZM et al., 2017; Gou ZB et al., 2020). The age of the Ilam Nappe is about 39–19 Ma (Imayama T et al., 2022). The age of the Ama Drime Massif is 38–15 Ma (Wang XX et al., 2017; Wang JM et al., 2021). The ages observed in central Nepal are 35–16 Ma (Kohn MJ, 2014). The age of Nyalam is 32–14 Ma (Wang JM et al., 2015, 2016). The age of Zanskar in the western Himalayan segment is 44–22 Ma (Štípská P et al., 2020). In addition, the partial melting time of the GHC in the Gyirong area is 29–18 Ma, and the temperature and pressure ranges are 640–720°C and 600–1200 MPa, respectively (Khanal GP et al., 2020). The ages of zircons in the GHC schist, leucogranite, and pegmatite in the Gyirong area all indicate that the study area has undergone long-term partial melting, with an age range of 39–16 Ma (Fig. 8). The above studies indicate that although the start and end times of metamorphism vary in different regions, they all indicate that the GHC experienced long-term metamorphism and partial melting from the late Eocene to the Miocene, with a duration of up to approximately 30 Ma (Weinberg RF, 2016;

Goscombe B et al., 2018; Zhang ZM et al., 2018; Mottram CM et al., 2019; Wang JM et al., 2017, 2022).

The U-Th-He ages of the zircons in the THS and the Malashan dome on the northern side of the study area are 36–32 Ma, and the apatite fission track ages are 9.6–7.2 Ma (Li G et al., 2018). The ages determined from zircon and apatite fission tracks from the Malashan dome to Gyirong County are mainly concentrated at 18–15 Ma (Shen T et al., 2016). The Ar-Ar age of muscovite from the two-mica granite at the top of the GHC in the northern part of the study area is 17.2–13.6 Ma (Zhang JJ et al., 2012), and the results of the Ar-Ar age of the Gyirong pegmatite in this study are in accordance with the above results (Fig. 7). The zircon and apatite fission track ages of the orthogneiss in the study area are 8.7 Ma and 1.9 Ma, respectively (Li M et al., 2013). Therefore, from north to south (from the THS to the GHC), the ages of the zircon and apatite fission tracks gradually become younger, and rapid uplift and denudation were concentrated in the middle and late Miocene. Therefore, this study suggests that a rapid exhumation process occurred at 16–15 Ma after the crystallization of the Gyirong pegmatite (Fig. 8b).

Based on the synthesis of our results and those of previous studies (Hodges KV, 2000; Kohn MJ, 2014; Wu FY et al., 2015; Zhang ZM et al., 2017; Goscombe B et al., 2018; Searle MP and Treloar PJ, 2019; Liu L et al., 2022; Cao HW et al., 2022a), the tectonic activity and magmatic rock evolution stages from the late Eocene to late Miocene in the Gyirong area are briefly discussed below. (1) In the Eocene–Oligocene (about 39–29 Ma), low–angle subduction of Indian continental crust occurred beneath the Lhasa Plate. The Himalaya was dominated by continuous crustal thickening under compressional conditions, and formed the Himalayan fault-fold belt. The GHC was dominated by Barrovian-type prograde metamorphism. (2) During the late Oligocene (29–25 Ma), this region reached peak metamorphic conditions. (3) The Miocene (25–17 Ma) was the main period for the formation of the Himalayan leucogranite. The Indian continental crust subducting beneath the Lhasa Plate broke off or rolled back, and the GHC and THS were mainly in an extensional setting. The STDS on the northern side of the GHC started to slip northward, the MCT on the southern side started to thrust southward, and the GHC between these two faults experienced exhumation and decompression-related retrograde metamorphism. Large-scale late Oligocene to middle Miocene leucogranites were formed by decompression melting of the GHC. (4) In the middle Miocene (17–16 Ma), the activity of the Himalayan leucogranite gradually weakened, and anatectic melt crystallization and emplacement in the Gyirong area occurred. In the middle to late Miocene (15–14 Ma), the Himalayan region changed from north–south extension to east-west extension, forming north–south rifts, which may be the tectonic mechanism for the rapid exhumation in the study area (Cao HW et al., 2022a; Wang JM et al., 2022). Therefore, the Gyirong pegmatite records the tectonic settings of crustal thickening (39–29 Ma) caused by thrusting and crustal thinning (28–15 Ma) caused by the detachment system in the Himalayan region (Fig. 8).

5.4. Metallogenetic potential of rare metals in pegmatite

Pegmatite is one of the main rock sources of rare metals (Yao CY et al., 2021; Li WY et al., 2022b; Li Y et al., 2022c; Zhang Z et al., 2022). In recent years, a great breakthrough has been made in rare metals prospecting in the Himalayan leucogranite-pegmatite belt, which has great prospecting potential (Cao HW et al., 2022a; Zhang Z et al., 2022). However, the concentrations of rare elements such as Li, Be, Cs, Nb, and Ta in the Gyirong pegmatite are relatively low, and the average values are only 12.45×10^{-6}, 4.65×10^{-6}, 9.64×10^{-6}, 0.91×10^{-6} and 0.18×10^{-6}, respectively. The above geochemical features suggest that the Gyirong pegmatite lacks mineralization potential for rare metals. This study believes that the Gyirong pegmatite belongs to an anatectic origin, not from the high differentiation evolution of granite. Further research is needed to determine whether anatectic pegmatite has lower metallogenic potential for rare metals than highly fractionated pegmatite (Knoll T et al., 2023; Zhao ZH and Yan S, 2023).

6. Conclusions

(i) The Gyirong pegmatite has high Si, Al, and K contents, a high Al saturation index and low Na, Ca, Fe, Mn, P, Mg and Ti contents. This pegmatite exhibits low ΣREEs and positive Eu anomalies. On the whole, the Gyirong pegmatite is enriched in Rb, Cs, U, K, Th, and Pb and depleted in Nb, Ta, Zr, Ti, Eu, Sr, and Ba. Rare metals such as Li, Be, Nb, and Ta have low mineralization potential.

(ii) The Gyirong pegmatite displays high whole-rock $^{87}Sr/^{86}Sr_{(16\ Ma)}$ and low $\varepsilon_{Nd(16\ Ma)}$ values, with average values of 0.762 and −16.0, respectively. The initial values of $^{208}Pb/^{204}Pb_{(16\ Ma)}$, $^{207}Pb/^{204}Pb_{(16\ Ma)}$ and $^{206}Pb/^{204}Pb_{(16\ Ma)}$ of the whole rock are relatively high, with average values of 39.72, 15.79 and 19.56, respectively, which are consistent with the composition of the GHC. The $\varepsilon_{Hf}(t)$ values of Cenozoic anatectic zircons vary slightly and are concentrated between −12 and −9 with an average of −11.4. In this contribution, this study believes that the Gyirong pegmatite represents a typical anatectic pegmatite derived from the GHC.

(iii) The final crystallization of the melt occurred in the Miocene (16.5 Ma). The Ar-Ar inverse isochron age of muscovite is 15.2 Ma, which is slightly later than the crystallization age, proving that a rapid exhumation process occurred in the Gyirong area at 16–15 Ma. The Gyirong pegmatite records long-term late Eocene–early Oligocene prograde metamorphism (about 39–29 Ma), late Oligocene peak metamorphism (29–25 Ma), and continuous Miocene retrograde metamorphism (25–17 Ma), as well as middle and late Miocene melt crystallization (17–16 Ma) and denudation-related cooling processes (16–15 Ma). The tectonic settings corresponding to the metamorphic and magmatic activity in the Himalayas are crustal thickening caused by thrust

compression at 39–29 Ma and crustal thinning caused by extensional decompression associated with the STDS during 28–15 Ma.

CRediT authorship contribution statement

Hua-wen Cao and Qiu-ming Pei designed and directed the project; Hua-wen Cao, Xiao-yu, Ai-bin Cao, Yong Cheng and Hang Liu carried out the field work and analysis of samples; Kai Zhang, Xin Liu, and Xiang-fei Zhang conducted the data analysis and the production of the drawings; Hua-wen Cao, Qiu-ming Pei and Xiao Yu wrote the article. All authors discussed the results and contributed to the final manuscript.

Declaration of Competing Interest

The authors declare no conflicts of interest.

Acknowledgment

This work was sponsored by the National Key R&D Programme of China (2021YFC2901803), National Natural Science Foundation of China (92055314 and 41802095), and the China Geological Survey (DD20230049 and DD20220983) and is a contribution to the International Geoscience Programme (IGCP-741) and Academician Bao-jun Liu Foundation of Southwest Geological Science and Technology Innovation Center. Drs. Huang Yong, Huang Han-xiao and Liu Hong participated in part of the field work. Dr. Jia-min Wang, one anonymous reviewer and Associate Editor Dr. Rui Wang provided valuable suggestions for revision. The authors wish to thank the laboratories for analyzing the samples in this contribution. Finally, the authors would like to thank the funding institutions for their strong support of this study.

Supplementary dataset

Supplementary data (Tables. S1–S6) to this article can be found online at doi: 10.31035/cg2022061.

References

Aleinikoff JN, Schenck WS, Plank MO, Srogi L, Fanning CM, Kamo SL, Bosbyshell H. 2006. Deciphering igneous and metamorphic events in high-grade rocks of the Wilmington Complex, Delaware: Morphology, cathodoluminescence and backscattered electron zoning, and SHRIMP U–Pb geochronology of zircon and monazite. GSA Bulletin, 118, 39–64. doi: 10.1130/b25659.1.

Ayres M, Harris N. 1997. REE fractionation and Nd-isotope disequilibrium during crustal anatexis: constraints from Himalayan leucogranites. Chemical Geology, 139, 249–269. doi: 10.1016/S0009-2541(97)00038-7.

Bhandari S, Qin K, Zhou Q, Evans NJ. 2022. Geological, Mineralogical and Geochemical Study of the Aquamarine-Bearing Yamrang Pegmatite, Eastern Nepal with Implications for Exploration Targeting. Minerals, 12, 564. doi: 10.3390/min12050564.

Burg JP, Bouilhol P. 2019. Timeline of the South-Tibet-Himalayan belt: the geochronological record of subduction, collision, and underthrusting from zircon and monazite U–Pb ages. Canadian Journal of Earth Sciences, 56, 1318–1332. doi: 10.1139/cjes-2018-0174.

Cao HW, Huang Y, Li GM, Zhang LK, Wu JY, Dong L, Dai ZW, Lu L. 2018. Late Triassic sedimentary records in the northern Tethyan Himalaya: tectonic link with Greater India. Geoscience Frontiers, 9, 273–291. doi: 10.1016/j.gsf.2017.04.001.

Cao HW, Li GM, Zhang LK, Dong L, Gao K, Dai ZW. 2020a. Monazite U–Th–Pb age of Liemai Eocene granites in the southern Tibet and its geological implications. Sedimentary Geology and Tethyan Geology, 40(2), 31–42 (in Chinese with English abstract).

Cao HW, Li GM, Zhang LK, Zhang XF, Yu X, Chen Y, Lin B, Pei QM, Tang L, Zou H. 2022b. Genesis of Himalayan leucogranite and its potentiality of rare metal mineralization. Sedimentary Geology and Tethyan Geology, 42(2), 189–211 (in Chinese with English abstract).

Cao HW, Li GM, Zhang RQ, Zhang YH, Zhang LK, Dai ZW, Zhang Z, Liang W, Dong SL, Xia XB. 2021. Genesis of the Cuonadong tin polymetallic deposit in the Tethyan Himalaya: Evidence from geology, geochronology, fluid inclusions and multiple isotopes. Gondwana Research, 92, 72–101. doi: 10.1016/j.gr.2020.12.020.

Cao HW, Li GM, Zhang Z, Zhang LK, Dong SL, Xia XB, Liang W, Fu JG, Huang Y, Xiang AP, Qing CS, Dai ZW, Pei QM, Zhang YH. 2020b. Miocene Sn polymetallic mineralization in the Tethyan Himalaya, southeastern Tibet: A case study of the Cuonadong deposit. Ore Geology Reviews, 119, 103403. doi: 10.1016/j.oregeorev.2020.103403.

Cao HW, Pei QM, Santosh M, Li GM, Zhang LK, Zhang XF, Zhang YH, Zou H, Dai ZW, Lin B, Tang L, Yu X. 2022a. Himalayan leucogranites: A review of geochemical and isotopic characteristics, timing of formation, genesis, and rare metal mineralization. Earth-Science Reviews, 234, 104229. doi: 10.1016/j.earscirev.2022.104229.

Carosi R, Montomoli C, Rubatto D, Visonà D. 2013. Leucogranite intruding the South Tibetan Detachment in western Nepal: implications for exhumation models in the Himalayas. Terra Nova, 25, 478–489. doi: 10.1111/ter.12062.

Černý P, Ercit TS. 2005. The classification of granitic pegmatites revisited. The Canadian Mineralogist, 43, 2005–2026. doi: 10.2113/gscanmin.43.6.2005.

Chen RX, Zheng YF. 2017. Metamorphic zirconology of continental subduction zones. Journal of Asian Earth Sciences, 145, 149–176. doi: 10.1016/j.jseaes.2017.04.029.

Chen S, Zhang B, Zhang J, Wang Y, Li X, Zhang L, Yan Y, Cai F, Yue Y. 2022. Tectonic transformation from orogen-perpendicular to orogen-parallel extension in the North Himalayan Gneiss Domes: Evidence from a structural, kinematic, and geochronological investigation of the Ramba gneiss dome. Journal of Structural Geology, 155, 104527. doi: 10.1016/j.jsg.2022.104527.

Chen SS, Fan WM, Shi RD, Xu JF, Liu YM. 2021. The Tethyan Himalaya igneous province: Early melting products of the Kerguelen mantle plume. Journal of petrology, 62, egab069. doi: 10.1093/petrology/egab069.

Corfu F, Hanchar JM, Hoskin PWO, Kinny PD. 2003. Atlas of zircon textures. Reviews in Mineralogy and Geochemistry, 53, 469–500. doi: 10.2113/0530469.

Cottle J, Lederer G, Larson K. 2019. The monazite record of pluton assembly: Mapping manaslu using petrochronology. Chemical Geology, 530, 119309. doi: 10.1016/j.chemgeo.2019.119309.

Cottle JM, Larson KP, Yakymchuk C. 2018. Contrasting accessory mineral behavior in minimum-temperature melts: Empirical constraints from the Himalayan metamorphic core. Lithos, 312–313, 57–71. doi:10.1016/j.lithos.2018.05.003

Debon F, Le Fort P. 1983. A chemical-mineralogical classification of common plutonic rocks and associations. Transactions of the Royal Society of Edinburgh:Earth Sciences, 73, 135–149. doi: 10.1017/S0263593300010117.

Debon F, Le Fort P. 1988. A cationic classification of common plutonic rocks and their magmatic associations: principles, method, applications. Bulletin de Minéralogie, 111, 493–510.

Dill HG. 2015. Pegmatites and aplites: Their genetic and applied ore geology. Ore Geology Reviews, 69, 417–561. doi: 10.1016/j.oregeorev.2015.02.022.

Dill HG. 2018. Geology and chemistry of Variscan-type pegmatite systems (SE Germany)-With special reference to structural and chemical pattern recognition of felsic mobile components in the crust. Ore Geology Reviews, 92, 205–239. doi: 10.1016/j.oregeorev.2017.11.016.

Ding H, Zhang Z, Kohn MJ, Gou Z. 2021. Timescales of partial melting and melt crystallization in the Eastern Himalayan orogen: Insights from zircon petrochronology. Geochemistry, Geophysics, Geosystems, 22, e2020GC009539. doi: 10.1029/2020GC009539.

Ding L, Kapp P, Cai F, Garzione CN, Xiong Z, Wang H, Wang C. 2022. Timing and mechanisms of Tibetan Plateau uplift. Nature Reviews Earth and and Environment, 3, 652–667. doi: 10.1038/s43017-022-00318-4.

Ferry JM, Watson EB. 2007. New thermodynamic models and revised calibrations for the Ti-in-zircon and Zr-in-rutile thermometers. Contributions to Mineralogy and Petrology, 154, 429–437. doi: 10.1007/s00410-007-0201-0.

Fletcher IR, McNaughton NJ, Aleinikoff JA, Rasmussen B, Kamo SL. 2004. Improved calibration procedures and new standards for U–Pb and Th –Pb dating of Phanerozoic xenotime by ion microprobe. Chemical Geology, 209, 295–314. doi: 10.1016/j.chemgeo.2004.06.015.

Frost CD, Frost BR. 2011. On ferroan (A-type) granitoids: their compositional variability and modes of origin. Journal of petrology, 52, 39–53. doi: 10.1093/petrology/egq070.

Gao LE, Zeng LS, Asimow PD. 2017. Contrasting geochemical signatures of fluid-absent versus fluid-fluxed melting of muscovite in metasedimentary sources: The Himalayan leucogranites. Geology, 45, 39–42. doi: 10.1130/g38336.1.

Gao LE, Zeng LS, Wang L, Hou KJ, Gao JH, Shang Z. 2016. Timing of different crustal partial melting in the Himalayan orogenic belt and its tectonic implications. Acta Geologica Sinica, 90(11), 3039–3059 (in Chinese with English abstract).

Gao LE, Zeng LS, Zhao LH, Gao JH, Shang Z. 2021. Behavior of apatite in granitic melts derived from partial melting of muscovite in metasedimentary sources. China Geology, 4(1), 44–55. doi: 10.31035/cg2021009.

Gao LE, Zeng LS. 2014. Fluxed melting of metapelite and the formation of Miocene high-CaO two-mica granites in the Malashan gneiss dome, southern Tibet. Geochimica et Cosmochimica Acta, 130, 136–155. doi: 10.1016/j.gca.2014.01.003.

Goscombe B, Gray D, Foster DA. 2018. Metamorphic response to collision in the Central Himalayan Orogen. Gondwana Research, 57, 191–265. doi: 10.1016/j.gr.2018.02.002.

Gou ZB, Dong X, Wang BD. 2019. Petrogenesis and tectonic implications of the Paiku Leucogranites, Northern Himalaya. Journal of Earth Science, 30, 525–534. doi: 10.1007/s12583-019-1219-8.

Gou ZB, Liu H, Duan YY, Li J, Zhang SZ. 2020. Timescales of partial melting in Yadong region of higher Himalayan crystalline sequence: Constraints from zircon U–Pb geochronology of Naiduila Migmatites. Earth Science, 45(8), 2894–2904 (in Chinese with English abstract).

Gou ZB, Liu H, Li J, Zhang SZ, Zhao XD, Wang SW. 2022. Petrogenesis and geological implications of the Yadong Migmatites, South Tibet. Sedimentary Geology and Tethyan Geology, 42(2), 279–287 (in Chinese with English abstract).

Gou ZB, Zhang ZM, Dong X, Xiang H, Ding HX, Tian ZL, Lei HC. 2016. Petrogenesis and tectonic implications of the Yadong leucogranites, southern Himalaya. Lithos, 256–257, 300–310. doi: 10.1016/j.lithos.2016.04.009.

Harris N, Ayres M. 1998. The implications of Sr-isotope disequilibrium for rates of prograde metamorphism and melt extraction in anatectic terrains. Geological Society, London, Special Publications, 138, 171-182. doi: 10.1144/gsl.Sp.1996.138.01.10.

Hodges KV. 2000. Tectonics of the Himalaya and southern Tibet from two perspectives. Geological Society of America Bulletin, 112, 324–350. doi: 10.1130/0016-7606(2000)112<324:TOTHAS>2.0.CO;2.

Hu XM, Garzanti E, Wang JG, Huang WT, An W, Webb A. 2016. The timing of India-Asia collision onset-facts, theories, controversies. Earth-Science Reviews, 160, 264–299. doi: 10.1016/j.earscirev.2016.07.014.

Hu Z, Liu Y, Gao S, Liu W, Zhang W, Tong X, Lin L, Zong K, Li M, Chen H, Zhou L, Yang L. 2012. Improved in situ Hf isotope ratio analysis of zircon using newly designed X skimmer cone and jet sample cone in combination with the addition of nitrogen by laser ablation multiple collector ICP-MS. Journal of Analytical Atomic Spectrometry, 27, 1391–1399. doi: 10.1039/C2JA30078H.

Hu Z, Zhang W, Liu Y, Gao S, Li M, Zong K, Chen H, Hu S. 2015. "Wave" signal-smoothing and mercury-removing device for laser ablation Quadrupole and multiple collector ICPMS analysis: Application to Lead Isotope analysis. Analytical Chemistry, 87, 1152–1157. doi: 10.1021/ac503749k.

Huang Y, Cao HW, Li GM, Brueckner SM, Zhang Z, Dong L, Dai ZW, Lu L, Li YB. 2018. Middle-late Triassic bimodal intrusive rocks from the Tethyan Himalaya in South Tibet: Geochronology, petrogenesis and tectonic implications. Lithos, 318–319, 78–90. doi: 10.1016/j.lithos.2018.08.002.

Imayama T, Arita K, Fukuyama M, Yi K, Kawabata R. 2019. 1.74 Ga crustal melting after rifting at the northern Indian margin: investigation of mylonitic orthogneisses in the Kathmandu area, central Nepal. International Geology Review, 61, 1207–1221. doi: 10.1080/00206814.2018.1504329.

Imayama T, Hoshino R, Yi K, Kawabata R. 2022. Eocene to Miocene metamorphic evolution and tectonic implication of the Ilam Nappe in Nepal Himalaya: Constraints from P-T conditions and monazite petrochronology. Journal of Asian Earth Sciences, 105276. doi: 10.1016/j.jseaes.2022.105276.

Irber W. 1999. The lanthanide tetrad effect and its correlation with K/Rb, Eu/Eu*, Sr/Eu, Y/Ho, and Zr/Hf of evolving peraluminous granite suites. Geochimica et Cosmochimica Acta, 63, 489–508. doi: 10.1016/s0016-7037(99)00027-7.

Jackson SE, Pearson NJ, Griffin WL, Belousova EA. 2004. The application of laser ablation-inductively coupled plasma-mass spectrometry to in situ U –Pb zircon geochronology. Chemical Geology, 211, 47–69. doi: 10.1016/j.chemgeo.2004.06.017.

Kang DY, Zhang ZM, Palin RM, Tian ZL, Dong X. 2020. Prolonged partial melting of garnet amphibolite from the Eastern Himalayan syntaxis: Implications for the tectonic evolution of large hot Orogens. Journal of Geophysical Research:Solid Earth, 125, e2019JB019119. doi: 10.1029/2019jb019119.

Kellett DA, Grujic D, Coutand I, Cottle J, Mukul M. 2013. The South Tibetan detachment system facilitates ultra rapidultra-rapid cooling of granulite-facies rocks in Sikkim Himalaya. Tectonics, 32, 252–270. doi: 10.1002/tect.20014.

Khanal GP, Wang JM, Wu FY, Wang JG, Yang L. 2020. In-sequence buoyancy extrusion of the Himalayan Metamorphic Core, central Nepal: Constraints from monazite petrochronology and thermobarometry. Journal of Asian Earth Sciences, 199, 104406. doi: 10.1016/j.jseaes.2020.104406.

Knoll T, Huet B, Schuster R, Mali H, Ntaflos T, Hauzenberger C. 2023. Lithium pegmatite of anatectic origin-A case study from the Austroalpine Unit Pegmatite Province (Eastern European Alps): geological data and geochemical model. Ore Geology Reviews, 105298. doi: 10.1016/j.oregeorev.2023.105298.

Kohn MJ. 2014. Himalayan metamorphism and its tectonic implications.

Annual Review of Earth and Planetary Sciences, 42, 381–419. doi: 10.1146/annurev-earth-060313-055005.

Koppers AAP. 2002. ArArCALC-software for $^{40}Ar/^{39}Ar$ age calculations. Computers and and Geosciences, 28, 605–619. doi: 10.1016/S0098-3004(01)00095-4.

Larson KP, Cottle JM, Camacho A, Piercey S, Grujic D. 2022. Miocene anatexis, cooling and exhumation in the Khumbu Himal, Nepal. International Geology Review., 64(4), 12008–20336. doi: 10.1080/00206814.2021.1969524.

Le Fort P, Cuney M, Deniel C, France-Lanord C, Sheppard SMF, Upreti BN, Vidal P. 1987. Crustal generation of the Himalayan leucogranites. Tectonophysics, 134, 39–57. doi: 10.1016/0040-1951(87)90248-4.

Lederer GW, Cottle JM, Jessup MJ, Langille JM, Ahmad T. 2013. Timescales of partial melting in the Himalayan middle crust: Insight from the Leo Pargil dome, northwest India. Contributions to Mineralogy and Petrology, 166, 1415–1441. doi: 10.1007/s00410-013-0935-9.

Leloup PH, Liu X, Mahéo G, Paquette JL, Arnaud N, Aubray A, Liu X. 2015. New constraints on the timing of partial melting and deformation along the Nyalam section (central Himalaya): Implications for extrusion models. Geological Society, London, Special Publications, 412, 131–175. doi: 10.1144/sp412.11.

Li GW, Kohn B, Sandiford M, Ma ZL, Xu ZQ. 2018. Post-collisional exhumation of the Indus-Yarlung suture zone and Northern Tethyan Himalaya, Saga, SW Tibet. Gondwana Research. 64, 1–10. doi: 10.1016/j.gr.2018.06.006.

Li M, Wang A, Liu C, Wang GC, Li T, Garver JI. 2013. Neogene exhumation of the Greater Himalaya Slab in Gyirong area, Tibet, constrained by fission track geochronology. Geological Bulletin of China, 2013,32(1), 86–92 (in Chinese with English abstract).

Li WY, Zhang ZW, Gao YB, Hong J, Chen B, Zhang ZB. 2022b. Tectonic transformation of the Kunlun Paleo-Tethyan orogenic belt and related mineralization of critical mineral resources of nickel, cobalt, manganese and lithium. Geology in China, 49(5), 1385–1407 (in Chinese with English abstract).

Li X, Zheng YC, Yang ZS, Hou ZQ, Wu CD, Xu PY, Wang L. 2022a. Discovery of Miocene pegmatite type Be–Nb–Ta(–Rb) mineralization in the Yangbajain of Central Lhasa subterrane, Tibet. China Geology, 5(4), 768–770. doi: 10.31035/cg2022037.

Li Y, Wang W, Du XF, Chen ZL, Ma HD, Qiu L, Liu W, Zhang YF, Huo HL. 2022c. $^{40}Ar/^{39}Ar$ dating of muscovite of the west 509 Daoban Li-Be rare metal deposit in the West Kunlun orogenic belt and its limitation to regional mineralization. Geology in China, 49(6), 2031–2033 (in Chinese with English abstract).

Lin C, Zhang J, Wang X, Putthapiban P, Zhang B, Liu K, Huang T. 2020. Late triassic back-arc spreading and initial opening of the Neo-Tethyan Ocean in the northern margin of Gondwana: Evidences from Late Triassic BABB-type basalts in the Tethyan Himalaya, Southern Tibet. Lithos, 358–359, 105408. doi: 10.1016/j.lithos.2020.105408.

Linnen RL, Van Lichtervelde M, Cerny P. 2012. Granitic pegmatites as sources of strategic metals. Elements, 8, 275–280. doi: 10.2113/gselements.8.4.275.

Liu C, Wang RC, Wu FY, Xie L, Liu XC, Li XK, Yang L, Li XJ. 2020. Spodumene pegmatites from the Pusila pluton in the higher Himalaya, South Tibet: Lithium mineralization in a highly fractionated leucogranite batholith. Lithos, 358–359, 105421. doi: 10.1016/j.lithos.2020.105421

Liu L, Zhu DC, Wang Q, Cawood PA, Stockli DF, Stockli LD, Lin C, Zhang JJ, Zhang LL, Zhao ZD. 2022. Leucogranite records multiple collisional orogenies. Geophysical Research Letters, 49, e2021GL096817. doi: 10.1029/2021GL096817.

Liu YS, Hu Z, Zong K, Gao C, Gao S, Xu J, Chen H. 2010. Reappraisement and refinement of zircon U–Pb isotope and trace element analyses by LA-ICP-MS. Chinese Science Bulletin, 55, 1535–1546. doi: 10.1007/s11434-010-3052-4.

Liu ZC, Wu FY, Guo CL, Zhao ZF, Yang JH, Sun JF. 2011. In situ U–Pb dating of xenotime by laser ablation (LA)–ICP–MS. Chinese Science Bulletin, 56, 2948–2956. doi: 10.1007/s11434-011-4657-y.

London D, Kontak DJ. 2012. Granitic Pegmatites: Scientific wonders and economic Bonanzas. Elements, 8, 257–261. doi: 10.2113/gselements.8.4.257.

London D, Morgan GB. 2012. The pegmatite puzzle. Elements, 8, 263–268. doi: 10.2113/gselements.8.4.263.

London D. 2018. Ore-forming processes within granitic pegmatites. Ore Geology Reviews, 101, 349–383. doi: 10.1016/j.oregeorev.2018.04.020.

Ludwig KR. 2012. User's Manual for Isoplot 3.75: A geochronological toolkit for Microsoft Excel. Berkeley Geochronology Center, Berkeley. 1–66.

Luo T, Hu Z, Zhang W, Günther D, Liu Y, Zong K, Hu S. 2018a. Reassessment of the influence of carrier gases He and Ar on signal intensities in 193 nm excimer LA–ICP–MS analysis. Journal of Analytical Atomic Spectrometry, 33, 1655–1663. doi: 10.1039/C8JA00163D.

Luo T, Hu Z, Zhang W, Liu Y, Zong K, Zhou L, Zhang J, Hu S. 2018b. Water vapor-assisted "Universal" nonmatrix-matched analytical method for the *in situ* U–Pb sating of Zircon, Monazite, Titanite and Xenotime by laser ablation-inductively coupled plasma mass spectrometry. Analytical Chemistry, 90, 9016–9024. doi: 10.1021/acs.analchem.8b01231.

Luo T, Zhao H, Li Q, Li Y, Zhang W, Guo J, Liu Y, Zhang J, Hu Z. 2020. Non-matrix-matched determination of Th-Pb ages in zircon, monazite and xenotime by laser Ablation-inductively coupled plasma-mass apectrometry. Geostandards and Geoanalytical Research, 44, 653–668. doi: 10.1111/ggr.12356.

Ma ZN, Han ZP, Li YL, Bi WJ, Xu TK, Xiao SQ. 2022. Exhumation history of the Kampa dome in the southern Tibet: Evidence from low temperature thermochronology. Sedimentary Geology and Tethyan Geology, 42(2), 300–309 (in Chinese with English abstract).

Maniar PD, Piccoli PM. 1989. Tectonic discrimination of granitoids. Geological Society of America Bulletin, 101, 635–643. doi: 10.1130/0016-7606(1989)101<0635:TDOG>2.3.CO;2.

Martin AJ. 2017. A review of Himalayan stratigraphy, magmatism, and structure. Gondwana Research, 49, 42–80. doi: 10.1016/j.gr.2017.04.031.

McDonough WF, Sun SS. 1995. The composition of the Earth. Chemical Geology, 120, 223–253. doi: 10.1016/0009-2541(94)00140-4.

Metcalfe I. 2021. Multiple Tethyan Ocean basins and orogenic belts in Asia. Gondwana Research, 100, 87–130. doi: 10.1016/j.gr.2021.01.012.

Montel JM. 1993. A model for monazite/melt equilibrium and application to the generation of granitic magmas. Chemical Geology, 110, 127–146. doi: 10.1016/0009-2541(93)90250-M.

Morel MLA, Nebel O, Nebel-Jacobsen YJ, Miller JS, Vroon PZ. 2008. Hafnium isotope characterization of the GJ-1 zircon reference material by solution and laser-ablation MC-ICPMS. Chemical Geology, 255, 231–235. doi: 10.1016/j.chemgeo.2008.06.040.

Mottram CM, Cottle J, Kylander-Clark A. 2019. Campaign-style U–Pb titanite petrochronology; along-strike variations in timing of metamorphism in the Himalayan Metamorphic Core. Geoscience Frontiers, 10, 827–847. doi: 10.1016/j.gsf.2018.09.007.

Müller A, Romer RL, Pedersen RB. 2017. The sveconorwegian pegmatite province-thousands of pegmatites without parental granites. The Canadian Mineralogist, 55, 283–315. doi: 10.3749/canmin.1600075.

Müller A, Simmons W, Beurlen H, Thomas R, Ihlen PM, Wise M, Roda-Robles E, Neiva AMR, Zagorsky V. 2022. A proposed new mineralogical classification system for granitic pegmatites-Part I:

History and the need for a new classification. The Canadian Mineralogist, 60, 203–227. doi: 10.3749/canmin.1700088.

Pan GT, Wang LQ, Li RS, Yuan SH, Ji WH, Yin FG, Zhang WP, Wang BD. 2012. Tectonic evolution of the Qinghai-Tibet Plateau. Journal of Asian Earth Sciences, 53, 3–14. doi: 10.1016/j.jseaes.2011.12.018.

Pan GT, Wang LQ, Yin FG, Geng QR, Li GM, Zhu DC. 2022. Researches on geological tectonic evolution of Tibetan Plateau: A review, recent advances, and directions in the future. Sedimentary Geology and Tethyan Geology, 42(2), 151–175 (in Chinese with English abstract).

Pei QM, Ma SB, Li CH, Liu F, Zhang YH, Xiao Y, Wang SM, Wu JF, Cao HW. 2023. *In-situ* boron isotope and chemical composition of tourmaline in the Gyirong pegmatite, southern Tibet: Implications for petrogenesis and magma source. Frontiers in Earth Science, 10, 1037727. doi: 10.3389/feart.2022.1037727.

Rubatto D. 2017. Zircon: The metamorphic mineral. Reviews in Mineralogy and Geochemistry, 83, 261–295. doi: 10.2138/rmg.2017.83.09.

Rudnick RL, Gao S. 2014. 4.1-Composition of the Continental Crust, In: Holland HD, Turekian KK. (Eds.), Treatise on Geochemistry (Second Edition). Elsevier, Oxford, 1–51. doi: 10.1016/B978-0-08-095975-7.00301-6.

Sang HQ, Wang F, He HY, Wang YL, Yang LK, Zhu RX. 2006. Intercalibration of ZBH-25 biotite reference material untilized for K-Ar and ^{40}Ar-^{39}Ar age determination. Acta Petrologica Sinica, 22(12), 3059–3078.

Searle MP, Crawford MB, Rex AJ. 1992. Field relations, geochemistry, origin and emplacement of the Baltoro granite, Central Karakoram. Transactions of the Royal Society of Edinburgh:Earth Sciences, 83, 519–538. doi: 10.1017/S0263593300005861.

Searle MP, Treloar PJ. 2019. An introduction to Himalayan tectonics: A modern synthesis. Geological Society, London, Special Publications, 483, 1–17. doi: 10.1144/sp483-2019-20.

Searle MP. 2019. Timing of subduction initiation, arc formation, ophiolite obduction and India-Asia collision in the Himalaya. Geological Society, London, Special Publications, 483, 19–37. doi: 10.1144/sp483.8.

Shellnutt JG. 2018. The Panjal Traps, In: Sensarma, S, Storey BC. (Eds.), Large Igneous Provinces from Gondwana and Adjacent Regions. Geological Society, London, Special Publications, 59–86. doi: 10.1144/sp463.4.

Shen T, Wang G, Leloup PH, van der Beek P, Bernet M, Cao K, Wang A, Liu C, Zhang K. 2016. Controls on Cenozoic exhumation of the Tethyan Himalaya from fission-track thermochronology and detrital zircon U–Pb geochronology in the Gyirong basin area, southern Tibet. Tectonics, 35, 1713–1734. doi: 10.1002/2016TC004149.

Sláma J, Košler J, Condon DJ, Crowley JL, Gerdes A, Hanchar JM, Horstwood MSA, Morris GA, Nasdala L, Norberg N, Schaltegger U, Schoene B, Tubrett MN, Whitehouse MJ. 2008. Plešovice zircon-A new natural reference material for U –Pb and Hf isotopic microanalysis. Chemical Geology, 249, 1–35. doi: 10.1016/j.chemgeo.2007.11.005.

Štípská P, Závada P, Collett S, Kylander Clark ARC, Hacker BR, Tabaud AS, Racek M. 2020. Eocene migmatite formation and diachronous burial revealed by petrochronology in NW Himalaya, Zanskar. Journal of Metamorphic Geology, 38, 655–691. doi: 10.1111/jmg.12534.

Sun SS, McDonough WF. 1989. Chemical and isotopic systematics of oceanic basalts: implications for mantle composition and processes. Geological Society, London, Special Publications, 42, 313–345. doi: 10.1144/GSL.SP.1989.042.01.19

Tian YH, Zeng LS, Gao LE, Wang YY, Hou KJ. 2021. Late Permian felsic magmatism along the Tethyan Himalaya, South Tibet and tectonic implications. Acta Petrologica Sinica, 37(10), 3035–3047 (in Chinese with English abstract). doi: 10.18654/1000-0569/2021.10.05.

Tomascak PB, Krogstad EJ, Walker JR. 1996. U–Pb monazite geochronology of granitic rocks from Maine: Implications for Late Paleozoic tectonics in the Northern Appalachians. The Journal of Geology, 104, 185–195. doi: 10.1086/629813.

Vermeesch P. 2018. IsoplotR: A free and open toolbox for geochronology. Geoscience Frontiers, 9, 1479–1493. doi: 10.1016/j.gsf.2018.04.001.

Wang JM, Lanari P, Wu FY, Zhang JJ, Khanal GP, Yang L. 2021. First evidence of eclogites overprinted by ultrahigh temperature metamorphism in Everest East, Himalaya: Implications for collisional tectonics on early Earth. Earth and Planetary Science Letters, 558, 116760. doi: 10.1016/j.epsl.2021.116760.

Wang JM, Rubatto D, Zhang JJ. 2015. Timing of partial melting and cooling across the Greater Himalayan Crystalline Complex (Nyalam, Central Himalaya): In-sequence thrusting and its implications. Journal of Petrology, 56, 1677–1702. doi: 10.1093/petrology/egv050.

Wang JM, Wu FY, Rubatto D, Liu SR, Zhang JJ, Liu XC, Yang L. 2017. Monazite behaviour during isothermal decompression in pelitic granulites: A case study from Dinggye, Tibetan Himalaya. Contributions to Mineralogy and Petrology, 172, 81. doi: 10.1007/s00410-017-1400-y.

Wang JM, Wu FY, Zhang JJ, Gautam K, Yang L. 2022. The Himalayan collisional orogeny: a metamorphic perspective. Acta Geologica Sinica, 96(9), 3128–3157 (in Chinese with English abstract).

Wang JM, Zhang JJ, Liu K, Zhang B, Wang XX, Rai S, Scheltens M. 2016. Spatial and temporal evolution of tectonometamorphic discontinuities in the central Himalaya: Constraints from P–T paths and geochronology. Tectonophysics, 679, 41–60. doi: 10.1016/j.tecto.2016.04.035.

Wang XX, Zhang JJ, Liu J, Yan SY, Wang JM. 2013. Middle-Miocene transformation of tectonic regime in the Himalayan orogen. Chinese Science Bulletin, 58, 108–117. doi: 10.1007/s11434-012-5414-6.

Wang XX, Zhang JJ, Yang XY. 2017. Geochemical characteristics of the Leucogranites from Gyirong, South Tibet: formation mechanism and tectonic implications. Geotectonica et Metallogenia, 41(2), 354–368.

Watson EB, Harrison TM. 1983. Zircon saturation revisited: Temperature and composition effects in a variety of crustal magma types. Earth and Planetary Science Letters, 64, 295–304. doi: 10.1016/0012-821X(83)90211-X.

Webb AAG, Guo H, Clift PD, Husson L, Müller T, Costantino D, Yin A, Xu Z, Cao H, Wang Q. 2017. The Himalaya in 3D: Slab dynamics controlled mountain building and monsoon intensification. Lithosphere, 9, 637–651. doi: 10.1130/l636.1.

Weinberg RF. 2016. Himalayan leucogranites and migmatites: Nature, timing and duration of anatexis. Journal of Metamorphic Geology, 34, 821–843. doi: 10.1111/jmg.12204.

Wiedenbeck M, Hanchar JM, Peck WH, Sylvester P, Valley J, Whitehouse M, Kronz A, Morishita Y, Nasdala L, Fiebig J, Franchi I, Girard JP, Greenwood RC, Hinton R, Kita N, Mason PRD, Norman M, Ogasawara M, Piccoli PM, Rhede D, Satoh H, Schulz-Dobrick B, Skår O, Spicuzza M, Terada K, Tindle A, Togashi S, Vennemann T, Xie Q, Zheng YF. 2004. Further characterisation of the 91500 zircon crystal. Geostandards and Geoanalytical Research, 28, 9–39. doi: 10.1111/j.1751-908X.2004.tb01041.x.

Wise MA, Müller A, Simmons WB. 2022. A proposed new mineralogical classification system for granitic pegmatites. The Canadian Mineralogist, 60, 229–248. doi: 10.3749/canmin.1800006.

Wolff R, Hölzer K, Hetzel R, Xu Q, Dunkl I, Anczkiewicz AA, Li Z. 2022. Spatially focused erosion in the High Himalaya and the geometry of the Main Himalayan Thrust in Central Nepal (85°E) from thermo-kinematic modeling of thermochronological data in the Gyirong region (southern China). Tectonophysics, 229378. doi:

10.1016/j.tecto.2022.229378.

Woodhead J, Hergt J, Shelley M, Eggins S, Kemp R. 2004. Zircon Hf-isotope analysis with an excimer laser, depth profiling, ablation of complex geometries, and concomitant age estimation. Chemical Geology, 209, 121–135. doi: 10.1016/j.chemgeo.2004.04.026.

Wu FY, Li XH, Zheng YF, Gao S. 2007. Lu-Hf isotopic systematics and their applications in petrology. Acta Petrologica Sinica, 23(2), 185–220.

Wu FY, Liu XC, Ji WQ. Wang JM, Yang L. 2017. Highly fractionated granites: Recognition and research. Science China Earth Sciences, 60, 1201–1219. doi: 10.1007/s11430-016-5139-1.

Wu FY, Liu XC, Liu ZC, Wang RC, Xie L, Wang JM, Ji WQ, Yang L, Liu C, Khanal GP, He SX. 2020. Highly fractionated Himalayan leucogranites and associated rare-metal mineralization. Lithos, 352–353, 105319. doi: 10.1016/j.lithos.2019.105319.

Wu FY, Liu ZC, Liu XC, Ji WQ. 2015. Himalayan leucogranite: Petrogenesis and implications to orogenesis and plateau uplift. Acta Petrologica Sinica, 31(1), 1–36 (in Chinese with English abstract).

Xu B, Hou ZQ, Griffin WL, Lu Y, Belousova E, Xu JF, O'Reilly SY. 2021a. Recycled volatiles determine fertility of porphyry deposits in collisional settings. American Mineralogist, 106, 656–661. doi: 10.2138/am-2021-7714.

Xu B, Hou ZQ, Griffin WL, Zheng YC, Wang T, Guo Z, Hou J, Santosh M, O'Reilly SY. 2021b. Cenozoic lithospheric architecture and metallogenesis in Southeastern Tibet. Earth-Science Reviews, 214, 103472. doi: 10.1016/j.earscirev.2020.103472.

Xu B, Hou ZQ, Griffin WL, Yu JX, Long T, Zhao Y, Wang T, Fu B, Belousova E, O'Reilly SY. 2022. Apatite halogens and Sr–O and zircon Hf–O isotopes: Recycled volatiles in Jurassic porphyry ore systems in southern Tibet. Chemical Geology, 605, 120924. doi: 10.1016/j.chemgeo.2022.120924.

Yang T, Ma Y, Bian W, Jin J, Zhang S, Wu H, Li H, Yang Z, Ding J. 2015. Paleomagnetic results from the Early Cretaceous Lakang Formation lavas: Constraints on the paleolatitude of the Tethyan Himalaya and the India-Asia collision. Earth and Planetary Science Letters, 428, 120–133. doi: 10.1016/j.epsl.2015.07.040.

Yang XY, Zhang JJ, Qi GW, Wang DC, Guo L, Li PY, Liu J. 2009. Structure and deformation around the Gyirong basin, north Himalaya, and onset of the south Tibetan detachment system. Science in China Series D:Earth Sciences, 52, 1046–1058. doi: 10.1007/s11430-009-0111-2.

Yao CY, Wang TG, Ni P, Yao ZY, Guo WM, Zhu YP, Wang W. 2021. Metallogenic types, characteristics and research progress of Nb-Ta deposits. Geology in China, 48(6), 1748–1758 (in Chinese with English abstract).

Yin A. 2006. Cenozoic tectonic evolution of the Himalayan orogen as constrained by along-strike variation of structural geometry, exhumation history, and foreland sedimentation. Earth-Science Reviews, 76, 1–131. doi: 10.1016/j.earscirev.2005.05.004.

Yu SM, Ma XD, Hu YC, Chen W, Liu QP, Song Y, Tang JX. 2022. Post-subdution evolution of the Northern Lhasa Terrane, Tibet: Constraints from geochemical anomalies, chronology and petrogeochemistry. China Geology, 5(1), 84–95. doi: 10.31035/cg2021045.

Zeng LS, Gao LE, Tang SH, Hou KJ, Guo CL, Hu GY. 2015. Eocene magmatism in the Tethyan Himalaya, southern Tibet. Geological Society, London, Special Publications, 412, 287–316. doi: 10.1144/SP412.8.

Zeng LS, Gao LE. 2017. Cenozoic crustal anatexis and the leucogranites in the Himalayan collisional orogenic belt. Acta Petrologica Sinica, 33(5), 1420–1444 (in Chinese with English abstract).

Zhang JJ, Santosh M, Wang XX, Guo L, Yang XY, Zhang B. 2012. Tectonics of the northern Himalaya since the India-Asia collision. Gondwana Research, 21, 939–960. doi: 10.1016/j.gr.2011.11.004.

Zhang LK, Li GM, Santosh M, Cao HW, Dong SL, Zhang Z, Fu JG, Xia XB. Huang, Y., Liang, W., Zhang, S. T., 2019. Cambrian magmatism in the Tethys Himalaya and implications for the evolution of the Proto-Tethys along the northern Gondwana margin: A case study and overview. Geological Journal, 54, 2545–2565. doi: 10.1002/gj.3311.

Zhang Z, Li GM, Zhang LK, Cao HW, Yang C, Huang Y, Liang W, Fu JG, Dong SL, Xia XB, Dai ZW. 2021. Neoproterozoic bimodal magmatism in the eastern Himalayan orogen: Tectonic implications for the Rodinia supercontinent evolution. Gondwana Research, 94, 87–105. doi: 10.1016/j.gr.2021.01.016.

Zhang Z, Li GM, Zhang LK. 2022. Exploration and research progresses of rare metals in Himalayan belt, Tibet. Sedimentary Geology and Tethyan Geology, 42(2), 176–188 (in Chinese with English abstract).

Zhang ZM, Ding HX, Palin RM, Dong X, Tian ZL, Kong DY, Jiang YY, Qin SK, Li WT. 2022. On the origin of high-pressure mafic granulite in the Eastern Himalayan Syntaxis: implications for the tectonic evolution of the Himalayan orogen. Gondwana Research, 104, 4–22. doi: 10.1016/j.gr.2021.05.011.

Zhang ZM, Dong X, Ding HX, Tian ZL, Xiang H. 2017. Metamorphism and partial melting of the Himalayan orogen. Acta Petrologica Sinica, 33(8), 2313–2341 (in Chinese with English abstract).

Zhang ZM, Kang DY, Ding HX, Tian ZZ, Dong X, Qin SK, Mu HC, Li MM. 2018. Partial melting of Himalayan orogen and formation mechanism of leucogranites. Earth Science, 43(1), 82–98 (in Chinese with English abstract).

Zhang ZM, Xiang H, Dong X, Ding HX, He ZY. 2015. Long-lived high-temperature granulite-facies metamorphism in the Eastern Himalayan orogen, south Tibet. Lithos, 212 –215, 1–15. doi: 10.1016/j.lithos.2014.10.009.

Zhang ZM, Xiang H, Dong X, Li WC, Ding HX, Gou ZB, Tian ZL. 2017. Oligocene HP metamorphism and anatexis of the Higher Himalayan Crystalline Sequence in Yadong region, east-central Himalaya. Gondwana Research, 41, 173–187. doi: 10.1016/j.gr.2015.03.002.

Zhao ZB, Li C, Ma XX. 2021. How does the elevation changing response to crustal thickening process in the central Tibetan Plateau since 120 Ma? China Geology, 4(1), 32–43. doi: 10.31035/cg2021013.

Zhao ZH, Chen HY, Han JS. 2022. Rare metal mineralization of the Mesozoic pegmatite in Altay orogeny, northern Xinjiang. Acta Scientiarum Naturalium Universitatis Sunyatseni, 61(1), 1–26 (in Chinese with English abstract).

Zhao ZH, Yan S. 2023. Some issues relevant to rare metal metallogeny of granitic pegmatites. Geotectonica et Metallogenia, 47(1), 1–41 (in Chinese with English abstract).

Zhou W, Xie L, Wang RC, Wu FY, Tian EN, Liu C, Liu XC. 2022. The study on the micas in the Gyirong leucogranite pegmatite from Himalaya: Implications for the lithium enrichment. Acta Petrologica Sinica, 38(7), 2153–2173 (in Chinese with English abstract). doi: 10.18654/1000-0569/2022.07.20.

Zhu DC, Chung SL, Mo XX, Zhao ZD, Niu Y, Song B, Yang YH. 2009. The 132 Ma Comei-Bunbury large igneous province: Remnants identified in present-day southeastern Tibet and southwestern Australia. Geology, 37, 583–586. doi: 10.1130/g30001a.1.